ABSTRACT

Title of dissertation: ONSET OF GRANULAR FLOWS
BY LOCAL AND GLOBAL FORCING

Masahiro Toiya, Doctor of Philosophy, 2006

Dissertation directed by: Professor Wolfgang Losert
Department of Physics, Institute for Research
in Electronics and Applied Physics and
Institute for Physical Sciences and Technology

This thesis focuses on the onset of granular flows and memory effects in granular materials under local and global forcing conditions. Global flows are induced in a shear cell of Taylor-Couette type by moving a boundary wall. We find that how a granular shear flow starts depends strongly on the prior shear direction. We observe that when the shear direction is reversed, the material goes through a transient period during which the material compacts, the shear force is small, and the shear band is wide. Three dimensional confocal imaging of particle rearrangements during shear reversal shows that bulk and surface flows are comparable. Local flows are induced by forcing a rod into a fluid immersed granular bed with various preparation methods. Particle rearrangements are observed in 3D by confocal microscopy and by moving a laser sheet through the sample. Image analysis indicates that rearrangements spread farthest not directly under the penetrometer but in a ring around the penetrometer. In addition, the direction of preformed stress chains in

the material influences the particle rearrangements. Material compressed from one side exhibits anisotropic particle rearrangements under penetrometer testing.

Particle rearrangements that do not lead to steady flows but overall increase in the packing fracion have also been investigated. Vibration-induced compaction of spherical grains indicates that in addition to the cage motion there are rare "jump" events in which a single particle moves significantly more compared to its neighbors. Although rare, such "jumps" play a significant role in the compaction of the material as a whole. Temperature cycling experiments show similar results. Compaction of material has also been observed in the the Couette cell. Repeated reversals or oscillations of the shear direction lead to additional compaction, which can be described by a stretched exponential, similar to compaction induced by tapping.

For 3D imaging of dry and non-transparent materials, X-ray microtomography is used. Images taken during the ongoing penetrometer studies of spherical particles and the lunar simulant JSC-1, along with an outline for future experiments are presented.

ONSET OF GRANULAR FLOWS BY LOCAL AND GLOBAL FORCING

by

Masahiro Toiya

Dissertation submitted to the Faculty of the Graduate School of the
University of Maryland, College Park in partial fulfillment
of the requirements for the degree of
Doctor of Philosophy
2006

Advisory Commmittee:

Professor Wolfgang Losert, Chair/Advisor
Professor Elias Balaras
Professor Daniel P. Lathrop
Professor Karen Prestegaard
Professor Rajarshi Roy

Dedication

This thesis is dedicated to H. Anthony Smith (1939-2005).

Acknowledgments

Many thanks to my advisor, Dr. Wolfgang Losert, for his guidance over the years. I am grateful also for the opportunities he has given me to present our work at numerous conferences and meetings. I was fortunate to have worked with a number of talented undergraduates chosen by Dr. Losert as well. Ricardo Pizarro has made impressive contributions to the shear cell experiment, particularly on the height measurement setup. A significant portion of the shear cell data was also contributed by Katie Newhall, who did a remarkable job as a summer REU student in 2004. Justin Senseney has patiently spent many hours gathering and analyzing the shear cell data as well.

The 3D imaging apparatus with a laser sheet was an idea I should have conceived a year sooner. Thanks to the helping hands of Andrew Pomerance and Steve Slotterback, I was able to include the preliminary results in this thesis.

My thesis committee members, Dr. Elias Balaras, Dr. Dan Lathrop, Dr. Karen Prestegaard, and Dr. Raj Roy had many helpful comments and suggestions. I am grateful for their cooperation.

Compaction studies and X-ray tomography experiments could not have been carried out without Professor Patrick Richard and Dr. Philippe Ribiere of Universite de Rennes I and Dr. Fabrice Barbe of INSA Rouen. As a colleague and a friend I would like to express my gratitude.

I owe special thanks to Don Martin. He has played an integral part in the

successful design and development of just about everything I have used for the research.

I would like to thank Justin Stambaugh, Kyuyong Lee, Erin Rericha, Mike Newey, Cory Poole, Sejin Han, Colin McCann, Matt Ferguson, Jennifer Galanis, Gene Kwon, Greg Bewley, and Jeff Harp for stimulating conversations and helpful comments.

I am truly grateful for encouragement and support from my parents, my sister Aiko, and my brother Hirokazu.

Thanks to my girlfriend, Linda, for patiently waiting for me to finish the Ph.D. program.

Table of Contents

List of Figures

Chapter 1

Introduction and Background

1.1 Overview: Granular Problems at Large

Granular materials are collections of particles in which the thermal energies of individual particles are negligible compared to typical kinetic or gravitational potential energies needed to move particles past one another. In this granular regime, the amount of energy needed to lift a particle by its diameter typically exceeds the particle's thermal energy by many orders of magnitude. Ranging in size from tens of microns to kilometers, granular materials can flow down a slope like a fluid, support large loads when packed tightly, and compact under moderate vibrations [4]. Wheat, rice, sugar, salt, sand, and gravel are examples which illustrate the ubiquitousness of granular materials.

Unique properties of granular materials in nature often manifest themselves in curious and complex phenomena such as migrating barchan sand dunes, rock avalanches (Fig. 1.1, Fig. 1.2. The origin of the recently discovered gullies on Mars such as the one shown in Fig. 1.1) is not clearly known. Liquid water flow, cyclic sublimation of atmospheric CO_2 and H_2O and dry granular flow are possible causes currently debated among researchers [10, 11]. Traditional Japanese landscaping techniques often employ sand gardens depicting lakes and mountains. Cohesive forces among wet sand grains arising from the surface tension of water are respon-

Figure 1.1: Crescent-shaped Barchan sand dune in Peru [1]. Width and height of these Barchans are of order 100m and 10m, respectively.

sible for retaining the shapes seen in Fig. 1.5. Shaken granular matter behaves like a gas but quickly loses kinetic energy through friction and inelastic collisions in the absence of continuous energy input. Therefore granular systems are in general out-of-equilibrium systems, and as such, traditional equilibrium statistical mechanics cannot fully describe them. A seemingly simple phenomenon such as sand avalanching down a slope, for example, consists of a liquid-like flowing portion at the top and a bulk of interlocking static particles underneath as shown in Fig. 1.4, with an angle of repose unique to each material and preparation method [12].

Reliable models of granular materials are needed in many areas of engineering. Polydisperse materials such as sand, gravel, or powdered pharmaceutical components tend to segregate based on grain size, posing a constant threat to any attempt for uniform mixing. Designs of commercial mixers are heavily researched and funded

Figure 1.2: Blackhawk landslide in southern California. Runout is approximately 3km wide and 10km long [2].

Figure 1.3: Gullies in Nirgal Vallis, Mars. Imaged region 2.3km wide by 2.8km long [3].

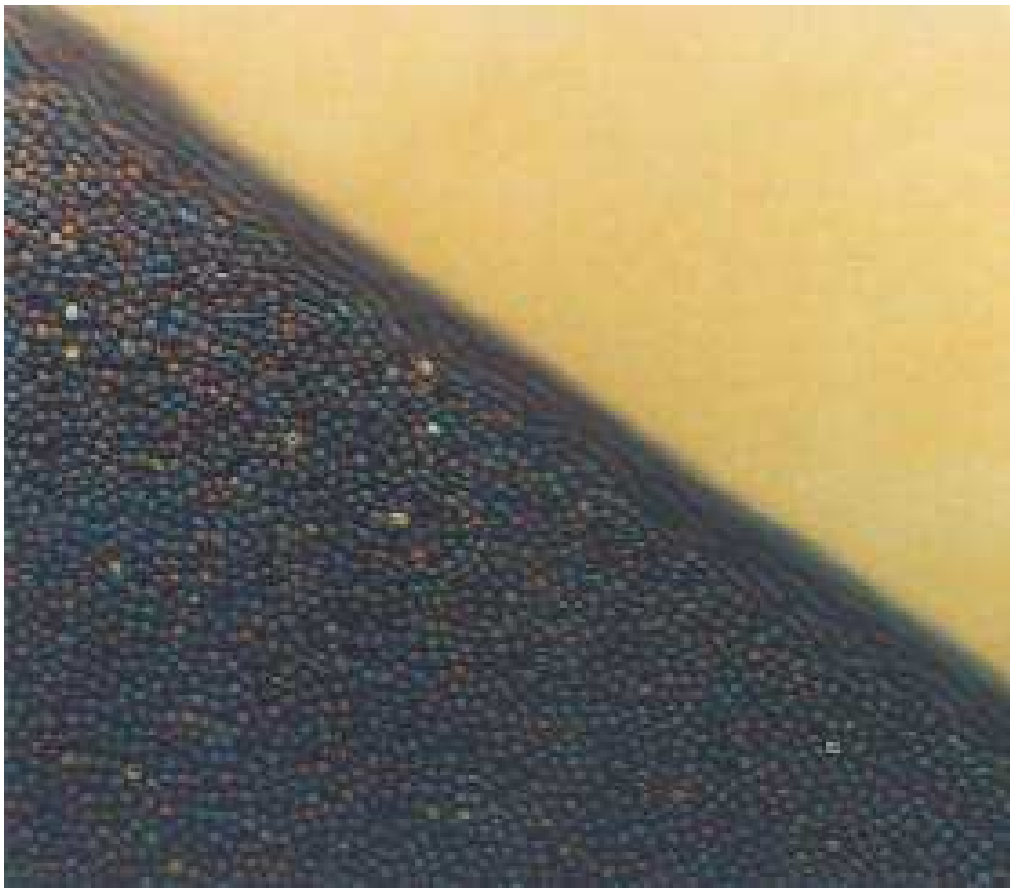

Figure 1.4: A granular avalanche [4]. Note the flowing layer near the surface and static bulk.

Figure 1.5: Sand garden at Ginkakuji temple in Kyoto, Japan. Sand is used to depict a lake and a mountain. Cohesive forces arising from the surface tension of water retain the shapes made with wet sand. Photo by M. Toiya.

Figure 1.6: Local jamming of grains resulted in uneven weight distribution, and eventually led to the collapse of this grain container [5].

by the pharmaceutical industry in which controlled mixing of drug components is of crucial importance [13]. Processing and transport of commercial granular materials mentioned above require understanding of the ways these material behave when subjected to various external forces. Here the complication lies in the fact that the materials undergo multiple phases during the journey from the source to the final destination: liquid-like flow during loading, compaction during transport due to vibrations, and dilation and flow once again when unloading. Size segregation, local or global jamming, and strengthening or weakening of the material can occur at each step and the consequences of equipment failure are are not only costly, but also sometimes harmful to the workers who handle these materials (Fig. 1.6).

Modeling difficulties stem from the intermediate state granular materials occupy among the traditional classification scheme of materials. The particles are large enough compared to the characteristic flow sizes, and continuum models such as modified forms of conventional fluid dynamics can offer only partial descriptions of granular behavior under limited circumstances. Currently subject to debate is whether this is due to a fundamental limitation of the analogy, or because a correct approach has not yet been found. Then there is the issue of scaling: One usually cannot extrapolate the behavior of a large granular systems from what one learns from a smaller system, making both a theoretical and computational approaches challenging.

These issues suggest that physical description of granular materials requires a multifaceted approach involving the physics of ordinary solids, liquids, and gases. Traditional engineering methods rely heavily on empirical data for accurate pre-

dictions of soil strength before construction, but when deciding on a location for a human habitat on the Moon or Mars, for example, there is often very limited amount, if any, of data on which predictions can be based. As such, the applicability of many empirical laws in environments vastly different from those on the earth is subject to debate. From predicting rock avalanches [2] and stability of grain elevators [14] to designing equipment for exploration of Martian deserts [15], the world is full of scientific and engineering challenges involving granular materials, where a reliable set of equations of motion, such as the Navier-Stokes equations in fluid mechanics, would prove valuable. The goal of this thesis is to characterize and bring forward some of the unique properties of granular materials at the crucial transition from jamming to flow with generic methods by which these materials are handled: shearing, local forcing by a rod, tapping, and temperature cycling.

1.2 Developments in Granular Experiments

In order to illustrate the complexity of phenomena observed in dense granular matter at the transition from jamming to flow, the so-called Brazil nut effect (BNE) serves as a good example. This is a simple and well-known phenomenon and the controversy over what the effect really entails, let alone its very existence, persists to this day. In the classic BNE, Brazil nuts are buried in a sea of smaller nuts. When the whole bulk is shaken, the larger Brazil nuts will somehow "float" on top of smaller nuts. The main cause of this effect is believed to be percolation: the shaking creates small gaps that are preferentially filled by small particles, the net effect being the

larger Brazil nuts rising to the top. But in 2001 molecular dynamics simulation results suggesting the *reverse* Brazil nut effect(RBNE), in which the larger particles "sink" to the bottom, was reported by Hong *et al* [16]. Their explanation was that condensation and percolation were the two competing components in segregation, and depending on the experimental conditions the effect could be reversed. In the RBNE, the authors claimed, the large particles enter condensed or solid state and sink to the bottom while the smaller particles remain fluidized. In a comment to the editor of the Physical Review Letters entitled "Does the Reverse Brazil Nut Effect Exist?", a group of experimentalists wrote that under laboratory conditions no such effect was observed [17]. The ensuing series of rather heated exchanges between the supporters of RBNE, theorists, simulation experts, and experimentalists in the granular physics community is indicative of the subtleties of granular (un)mixing problem involving merely two components [18, 19, 20].

One of the fundamental difficulties in granular experiments is that the precise determination of the 3D coordinates and velocities of individual grains is usually not possible. And since the universal governing equations are lacking, simulations do not properly reflect physical reality. Analysis of particle motion in 3D continues to be a challenge in the granular community. Many experimental findings are based on tracking particles in 2D geometries, i.e., in a single layer of grains with restricted freedom in the third dimension. 3D particle image velocimetry measurements excel at measuring bulk flow properties, but cannot study the individual particle-to-particle interactions. In most experimental setups with multiple layers of grains, observations are limited to the top surface of the bulk or side views through transparent

confining walls. Nevertheless, researchers have obtained valuable insights into the bulk behavior through surface measurements.

Intriguing features such as convection and size segregation have been observed in a Taylor Couette geometry by Behringer *et al.* [21]. Widening of the shear band, compaction, and weakening of material upon shear reversal observed mainly without 3D technique are reported in more detail in this thesis [8]. All of these phenomena have microscopic origins in the rearrangements of the grains. As we will show in this thesis, boundaries can also alter the velocity field in a granular flow - another motivation for development of 3d imaging techniques.

Preparation history of material has also been known to play a significant role in the compaction of granular packings. In the experiment where tapped granular materials were studied, the evolution of packing fraction was found to depend on the preparation method by which the initial packing fraction was achieved [22, 23]. In studies of geological events such as rock avalanches, the start of granular flow is of particular interest. It has been shown that in rock avalanches the prior history of shear forces applied to the soil may play a key role in determining the risk of such catastrophic flows. [2]. These results show that a global measure such as packing fraction alone is not sufficient for predicting the evolution of the system under tapping or shearing.

It is not surprising, then, that when direct observations of grains in 3D became possible a multitude of new breakthroughs occurred in short order. Magnetic Resonance Imaging (MRI) analysis of polydisperse grains in a rotating drum revealed the radial core consisting of small particles expanding toward the surface, giving rise

to the familiar alternating bands of small and large particles [24]. History dependence of shear flows has also been reported by Tsai, *et al.* [25], who measured the velocities of particles in the bulk as a function of depth in a Couette cell in which a weighted and rough top plate sheared the particles immersed in an index-matching fluid. The study found history dependent ordering and layering of their monodisperse grains over long timescales. Layering of particles and shear bands within the bulk of sheared grains have been observed by MRI and X-ray tomography [26]. The number of contacts per sphere under various packing fractions has been observed experimentally by X-ray tomography [27]. The distribution of interstitial void sizes have been predicted to take an exponential form [28], and confirmed by the X-ray tomography [29]. In the experiment detailed in [29], the exponential tail of the void size distribution dropped off much faster for higher packing fractions. Yet the pair-correlation function showed relatively small change, a subtle piece of evidence suggesting that the compaction is more than just decrease in mean distance between particles.

1.3 Scope of This Thesis

This thesis will explore the microscopic origins of granular behavior at the onset of flows due to external forcing. Various models to describe the steady and non steady state flow properties of granular matter have been developed [30, 31, 32, 33, 34]. In these models, the state of a system is characterized by density, granular temperature, and pressure. However, expanding flow models may not be sufficient

for the onset of a flow: The dynamics of granular matter at or close to rest have been shown to depend upon the history of applied forces [23, 35]. Furthermore, it is unclear how the empirical equations scale with gravity, which generally cannot be varied when the equations are tested. Hence, some combinations of density or velocity dependencies in empirical equations may in fact be based on dependencies on the gravitational force. Memory effects, particularly at the onset of flows, are explored in chapter 2. The model system used consists of spherical glass particles and cylindrical shear cell of Taylor-Couette type. Compaction, widening of shear band, and weakening of the material have been observed upon reversing the shear direction. In chapter 3 we investigate how granular materials fail under local forcing. A cylindrical rod is lowered into a mixture of index matching oil and dyed, transparent, non-spherical, and polydisperse particles. Imaging by confocal microscopy makes a 3D reconstruction possible, and reveals the displacement field of the mixture perturbed by the rod. While analysis by difference imaging does not track individual particles, the shear zone has the classic shape consistent with bearing capacity theory. By compressing the mixture from the side, stress chains are developed prior to perturbations by the rod. Results indicate that the displacement field spreads farther out along the preformed stress chains. Results obtained by oil immersed spherical particles with a new technique for imaging spherical particles in 3D are also presented. Volume scans are performed by sweeping a mixture of spherical grains and index matching oil with a laser sheet while imaging the fluorescent cross section. Advantages of 3D particle tracking and results with rod penetration experiments are discussed. Chapter 4 explores particle rearrangements that do

not lead to flow, but to compaction by vibration, temperature cycling, and oscillatory shear. Repeated thermal expansion and contraction of confining walls cause a packing of spherical particles to compact, via similar mechanism observed under tapping. We observe cage motion as well as "jumps", in which a particle finds a gap and moves significantly relative to its neighbors. Simulation with inhibited jumps show that the jumps play a significant role in the compaction of tapped granular media. Such events have also been seen in the temperature cycling experiments. Sidewall driven compaction, or repeated shear reversals in a Couette cell is also reported. Chapter 5 focuses on 3D imaging of dry and non-transparent materials with X-ray microtomography. Images taken during the ongoing penetrometer studies of spherical particles and the lunar simulant JSC-1, along with an outline for future experiments are presented.

Chapter 2

Steady-State and Transient Shear Flows

2.1 Chapter Overview

In this chapter, the onset of granular shear flows and its dependence on the history of prior stresses are investigated. In a granular assembly at rest, a network of contacting grains supports the applied stresses [36, 37, 7, 38]. The structure and failure of such networks are probed by applying controlled stresses and strains to the material while observing the resulting flow patterns. The experiments presented in the first parts of this chapter have been performed with spherical glass beads in a shear cell of Taylor-Couette type. Measured flow properties include the width of the region called shear band where the contact network fails, the packing fraction of the material, and the torque required for shearing. We find history dependence at the start of flow by shearing: Upon reversal of the shear direction the shear band widens, the material compacts, and the shear stress decreases. These transients gradually return to steady state flow over characteristic shear displacements involving the sizes of the system and the grains. The transient behavior during shear reversals is interpreted in the context of the force chains and the contact network introduced in Chapter 1. While most data on particle motion were obtained at the surface, we also observe shear banding in the interior of the granular bulk has been observed in fluid-immersed transparent particles. These tests indicate that the surface flows and

bulk behavior are similar. Some of the results presented here have been published in *Physical Review Letters* [8]. Others will be included in a second paper which is currently in preparation. These transient effects studied here at the onset of flows have particular relevance in understanding geophysical processes and also in civil engineering where transitions from jammed state to flowing state of soil particles are of major interest [2].

2.2 Background Information

2.2.1 Fluid Flow in A Cylindrical Taylor-Couette Geometry

The Taylor-Couette geometry is shown in Fig. 2.1. Granular material fills the gap between the two cylinders in our experiment. The rotating inner cylinder applies shear stress to the material. The Couette profile is the angular velocity profile of the sheared material as a function of the distance from the rotating wall. The Couette profile of a Newtonian fluid is described by,

$$V_\theta(r) = \frac{\omega a^2}{b^2 - a^2}\left[b^2/r^2 - 1\right]. \tag{2.1}$$

Fig. 2.2 shows the Couette profile of a Newtonian fluid and that of granular matter consisting of spherical glass beads (grain diameter $d = 1mm$, filling height $H = 118d$) from an actual experiment. In the granular system, the input energy is dissipated by friction in a narrow region near the inner cylinder, resulting in large velocity gradients near the inner cylinder. This localization of shearing is known as shear banding. Our investigation of shear banding of materials with different

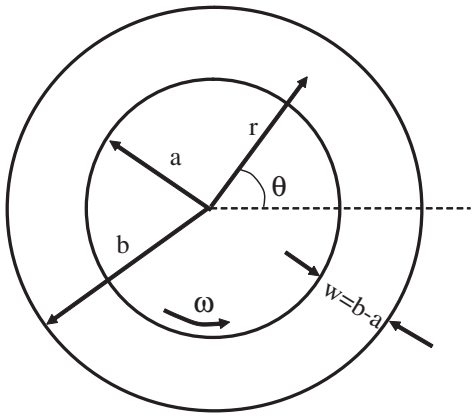

Figure 2.1: The Taylor-Couette geometry.

particle sizes and filling heights will be presented and interpreted in the following sections.

2.2.2 Review of Shear Testing in Soil Mechanics

We will start by examining a simpler shearing apparatus. Direct shear test is a standard method in geology and engineering by which shear strengths of soil samples are measured. A schematic shown in Fig. 2.3a describes the basic geometry. A typical model has the soil compartment sized 60mm square and 20mm deep. In this setup the lower part is pushed horizontally while a normal force N is applied in the vertical direction. The stress transmission can be visualized in simulations, for example in this discrete element model simulation by Hainbuchner *et al* [6]. Chains of particle contacts, along which forces are transmitted, are oriented roughly 45 degrees from the horizontal line along which the shear force is exerted. Here the thickness of the lines represents the magnitude of the force supported by that

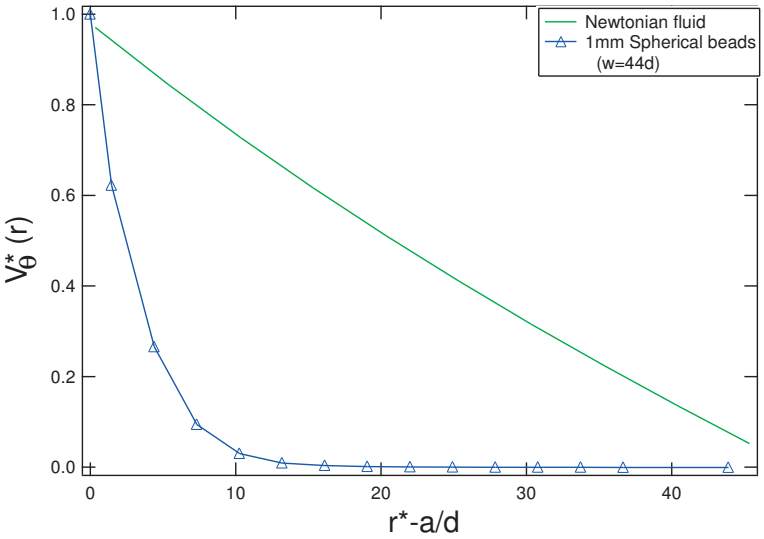

Figure 2.2: Angular velocity profile of a Newtonian fluid, shown along granular case in the same geometry. $V_\theta^* = V_\theta/\omega a$, and $r^* = r/d$, where d is the diameter of spherical grains. Local failure of the granular material near the inner wall is evident in this plot.

chain. As the shearing continues the chains appear and disappear, indicating the formation and breaking of contacts. The slightest motion of a single particle along a chain can alter the path of the force transmission non-linearly. Typical bulk stress-strain relationships are shown in Fig. 2.3c [39]. The stress is proportional to the strain during the initial transient period, indicating elastic deformations. If the shearing is reversed at any point during the test, weakening of the sample in the reversed direction is known to occur. This hysteresis is attributed to the crushing and repositioning of the particles [40], but this thesis we carry out a more quantitative analysis of this hysteresis in terms of the preferred direction of the contact network. Although continuous shearing is not possible with this setup, it is useful in characterizing the initial failure and weakening/strengthening due to shear reversals.

An analysis of static volume under stress provides another insight [40]. Fig. 2.4a shows a unit cube under stresses σ_1, σ_2, and σ_3. Normal and tangential components of the forces resulting from stresses on a plane oriented at angle α as shown in Fig. 2.4b are,

$$F_{normal} = \sigma_1 \cos\alpha \times area + \sigma_3 \sin\alpha \times area = \sigma_1 \cos\alpha + \sigma_3 \tan\alpha \sin\alpha, \tag{2.2}$$

$$F_{shear} = \sigma_1 \sin\alpha - \sigma_3 \tan\alpha \cos\alpha. \tag{2.3}$$

Dividing through by the cross sectional area of $1/\cos\alpha$, normal and shear stresses on a plane having the angle α as shown in the figure can be written as

$$\sigma_{normal} = \frac{\sigma_1 + \sigma_3}{2} + \frac{\sigma_1 - \sigma_3}{2} \cos 2\alpha, \tag{2.4}$$

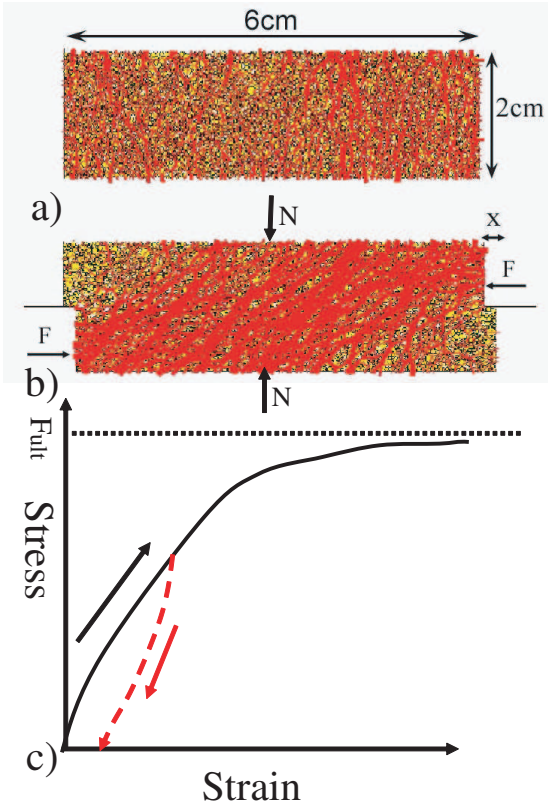

Figure 2.3: a), b) Discrete Element Method (DEM) simulation of direct shear test, performed by Hainbuchner, *et.al* [6]. A normal force N is applied to the sample while a shear force F is applied from the side. The observation that the force chains (shown in red) are oriented 45 degrees from the horizontal will be used in our model shown in Fig. 2.20. The stress/strain relation in c) shows that the stress increases and approaches F_{ult} as a function of strain. The soil type used in the testing determines the length scale of the curve. Note the hysteresis, or the memory effect, upon reversal of shear direction.

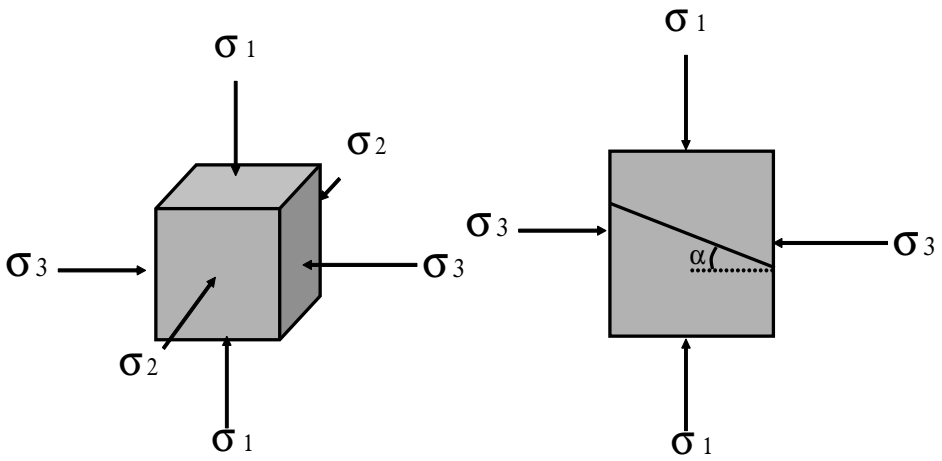

Figure 2.4: Confining stresses σ_1, σ_2, and σ_3 applied to a unit volume cause a net stress within the volume. Combined stresses result in maximum shear stress along a plane with $\alpha = 45$ degrees.

and

$$\sigma_{shear} = \frac{\sigma_1 - \sigma_3}{2} \sin 2\alpha. \tag{2.5}$$

Therefore the maximum shear stress in the static pile of grains is along the plane with $\alpha = 45$ and 135 degrees. We shall return to this observation later to explain the memory effect seen in our granular Taylor-Couette system.

2.2.3 Granular Shear Flows

Series of experiments to visualize stress chains in two dimensional granular assemblies have been carried out by Behringer *et al.*, in which photoelastic disks are used as grains [36, 37, 7, 38]. Polarization of these disks are sensitive to the applied stresses, and stress patterns emerge when viewed through crossed polarizers. As in the simulation result of the direct shear test shown in Fig. 2.3, the stress

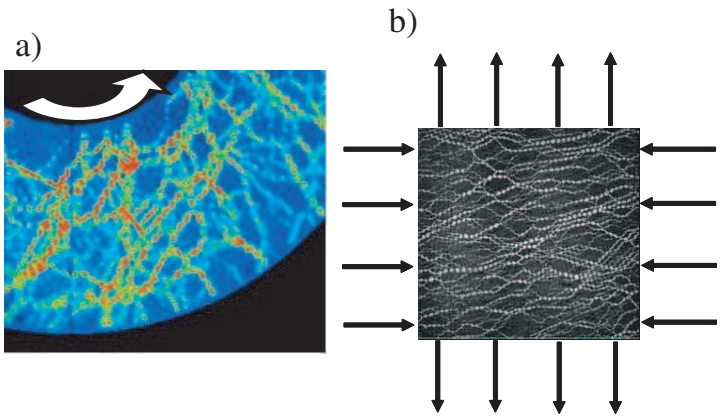

Figure 2.5: Examples of anisotropic stress chains. Note the orientation of force chains visualized by birefringent disks sheared in a Taylor-Couette cell (a). Results of pure shear in (b) indicate the force chains along the direction of compression. From [7].

chains extend roughly 45 degrees with respect to the direction of shear. Fig. 2.5a shows similar force chains. Fig. 2.5b shows the same grains undergoing pure shear. Force chains mostly orient themselves along the direction of compression, although some chains redirected toward the sidewalls are also visible [41, 7]. Other previous experiments with granular materials in a cylindrical shear cell with moving top plate include works by Tsai *et al.* [42, 25] in which crystallization transition and size segregation were reported. Losert *et al.* [34] used a Taylor-Couette geometry and upward air flow through the granular material, and reported a significant reduction in stick-slip motion and shear stress in their setup due to the forced air flow. Steady-state velocity profiles, velocity gradients, and local packing densities of grains in a Taylor-Couette shear cell have been performed with magnetic resonance imaging (MRI), X-ray tomography, and high-speed video particle tracking by Mueth, *et al* [26]. It was found that for deep filling of the shear cell, the velocity gradients

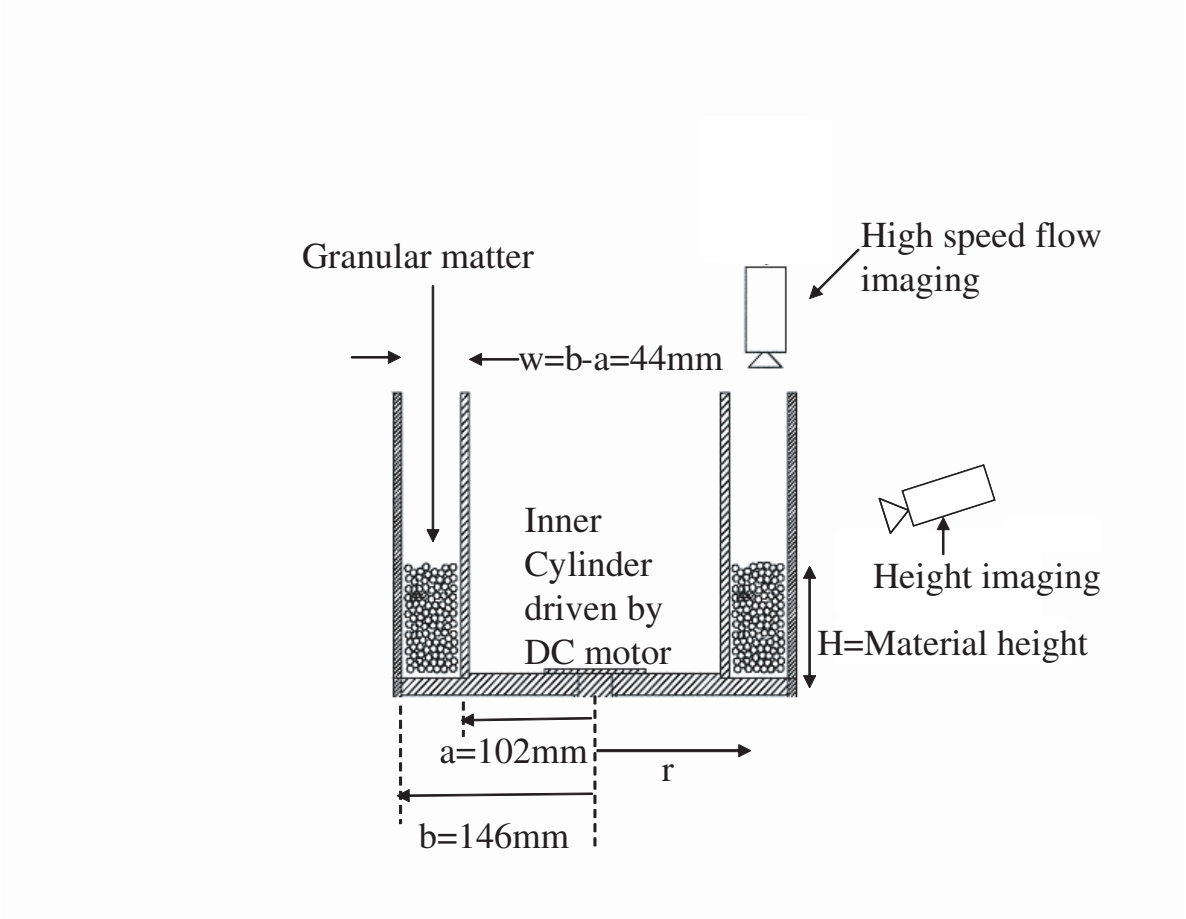

Figure 2.6: Schematic of the shear cell (side view). Granular matter is confined between the concentric cylinders.

are confined to several layers near the confining wall for a large range of materials tested.

2.3 Experimental Setup

Our experimental apparatus is shown in Fig. 2.6. It consists of two concentric cylinders of which the inner cylinder is driven by a variable speed DC servo motor. The bottom plate is attached to the inner cylinder. The outer cylinder is fixed. The

gap between the cylinders is filled with spherical glass beads of diameter $d = 1mm$, $d = 1.5mm$, $d = 2mm$, or $d = 3mm$, such that $w = 44d$, $w = 29d$, $w = 22d$, or $w = 14d$, respectively. A layer of glass beads of the same kind which fills the gap is glued to both cylinder surfaces and the bottom plate. Particles are added to the system through a funnel and a tube which extends to approximately 3cm from the top surface of the granular bed, while the inner cylinder continuously turns so that the material is distributed evenly.

The top surface of the granular material is imaged at up to 500 frames/s with a high speed camera mounted above the shear cell. A torque sensor positioned between the motor and the motor mount monitors the torque exerted on the inner cylinder. In a typical run the inner cylinder is rotated at 6-12 mHz, corresponding to a tangential velocity of 4-8 mm/sec. Particles on the top surface appear as bright spots in the images as shown in 2.7. A particle tracking algorithm in IDL identifies these bright spots, and tracks them from frame to frame. Images are taken at sufficiently high speed so that the particles travel less than 1/10 of a particle diameter between two consecutive frames.

Evolution of the packing fraction while shearing is monitored by simultaneously imaging particle motion and vertical dilation of the granular material as shown schematically in Figure 2.7. A thin strip of the top surface is illuminated and imaged from the side to capture the vertical position, i.e., height of the surface. A mirror positioned above the surface allows the camera to simultaneously capture the reflected images of the shear cell's top view. This allows for accurate measurements of the local height as a function of the displacement of the inner cylinder.

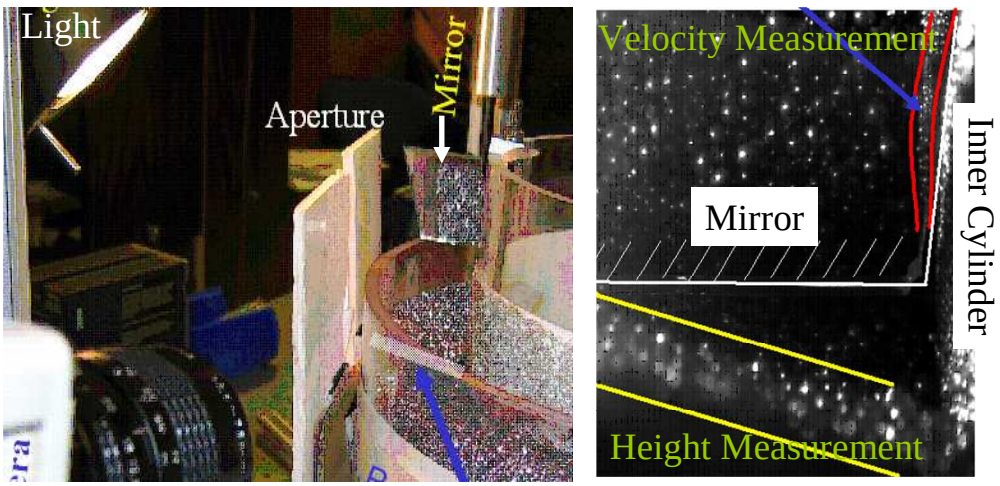

Figure 2.7: The filling height and the top view are simultaneously imaged in this setup. Camera captures the thin strip of light shining through a aperture slit across the top surface at an angle. The camera also captures the reflection of the top view from the mirror, to obtain accurate shear displacements.

The inner cylinder is rotated at a slow steady speed to prepare the particles in a reasonably consistent initial arrangement prior to the start of each run. We find that the start of shear flow is not strongly dependent on shear rate at the speeds we investigated from 0.3 mHz to 0.5 Hz. This is consistent with other findings for slow steady shear [41, 35, 26]. As will be described later, bidisperse mixtures segregate by particle size upon shearing, and for this reason the initialization is limited to 50 mm of shear displacement measured at the inner cylinder for runs with mixtures of particle sizes. Velocity profiles and torque measurements indicate that a steady state is reached within a shear displacement of 20 mm. The inner cylinder is stopped after initialization. Shear flow is initiated again by rotating the inner cylinder in the same or the opposite direction.

2.4 Results

2.4.1 Slow Steady Flow Regime: Continuous Breaking and Forming of Stress Network

Average velocities of particles are computed by dividing the width of the shear cell into four regions, as shown in Fig. 2.8a. Fig. 2.8b shows the average velocity vs. time in each of the four regions. The graph shows an experiment where the shear flow is suddenly started in the same direction as prior shear. We that a steady state tangential velocity profile is reached within a $1d$ after the shear cell is started in the same direction as the direction of prior shear. It also shows speeds after the shear cell is started in the opposite direction. One can see a transient state during which

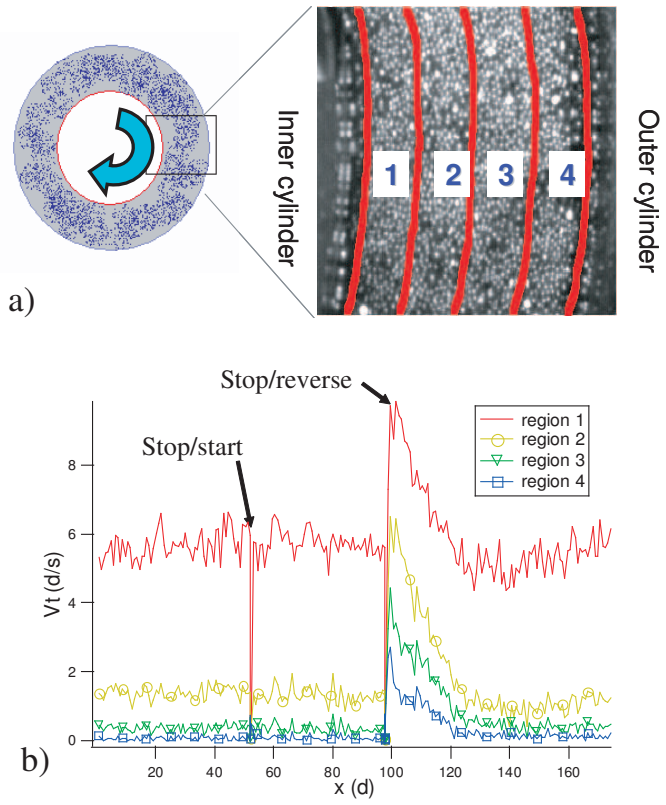

Figure 2.8: Imaged region is divided into four parts as shown in a) for calculations of average particle velocities. Average tangential velocities $|V_t|$ of $1mm$ particles vs. the inner cylinder displacement x is shown in b).

the shear band is wider and particles far from the inner cylinder move appreciably for a shear strain of $5 - 10d$ measured at the inner cylinder. Shear reversals will be treated in detail in the next section. These generic characteristics have been observed for all materials tested. Figs. 2.9, 2.10, 2.11 show the steady-state angular velocities plotted as a function of radial distance from the inner cylinder for various filling heights. The steady state velocities are computed from the averages over several hundred frames (shear displacements of$100d$ or greater). The imaging speed is chosen such that the particles do not move more than $\frac{1}{10}d$ between consec-

utive frames. The normalized angular velocities are given by $V_\theta^*(r) = V_\theta(r)/\omega$, and normalized radial coordinates from the center of the cylinders are given by $r^* = r/d$. For $w = 44d$ cases shown in Fig. 2.9, a nearly linear velocity profile over a width of approximately $20d$ is seen in the mid-section. For low filling heights, it is evident that the role of the bottom boundary is significant. For filling height of 90d and above, shearing near the inner wall dominates. The $w = 22d$ case (2.11, however, cannot have a 20d wide section, and tends to fail near the walls. To investigate further how the shear velocity profile depends on the width of the shear cell relative to the particle size, we investigate the shear band in detail.

We define the location of shear band in our shear cell as the location of the maximum in the absolute value of $\frac{dV_\theta}{dr}$. Figures 2.12˜ 2.14 show $\frac{dV_\theta}{dr}$ for $w = 44d$, $w = 29d$, and $w = 22d$, respectively. The locations of the dips in 2.12 indicate that the shear band approaches the inner wall as the filling height increases. The location of shear failure can thus be "tuned" with a characteristic width of the region of shear noted above. For a smaller particle size to system size ratio, the transition occurs not as a shifting of a notable shear band, but the shear appears distributed uniformly across the shear cell as shown in Figure 2.13. For $w = 29d$, two shear bands can exist simultaneously, as shown in Figs. 2.13. Since the only parameter varied are the particle size, we may conclude that the boundaries, i.e., the bottom and side surfaces, become more important for a smaller particle to system size ratio.

$\frac{dV_\theta}{dr}$ can be fitted to a gaussian with a width W and a peak position $(r - r_c/W)$.

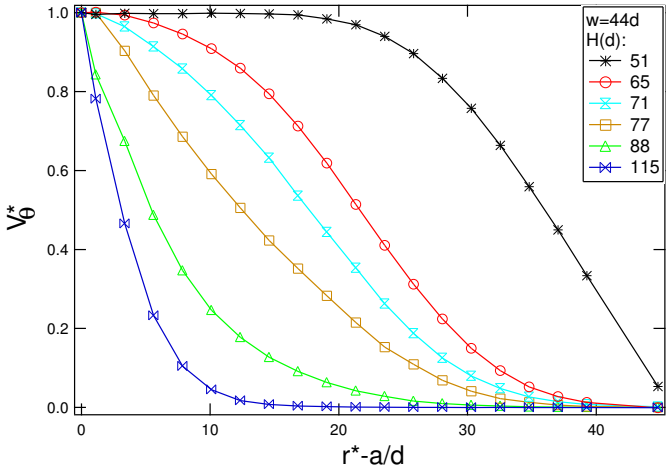

Figure 2.9: Steady state velocity profile for $w = 44d$ ($d = 1mm$). $V_\theta^* = V_\theta/\omega$, and $r^* = r/d$, where d is a particle diameter. Shear regions are approximately $20d$ wide and nearly linear, and their locations shift as a function of filling height.

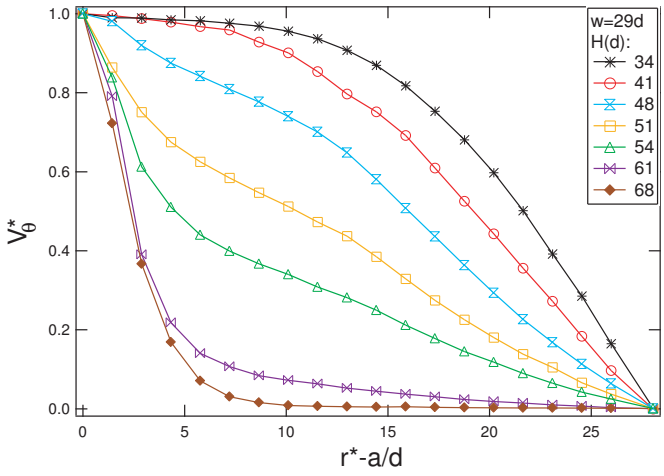

Figure 2.10: Steady state velocity profile for $w = 29d$ ($d = 1.5mm$).

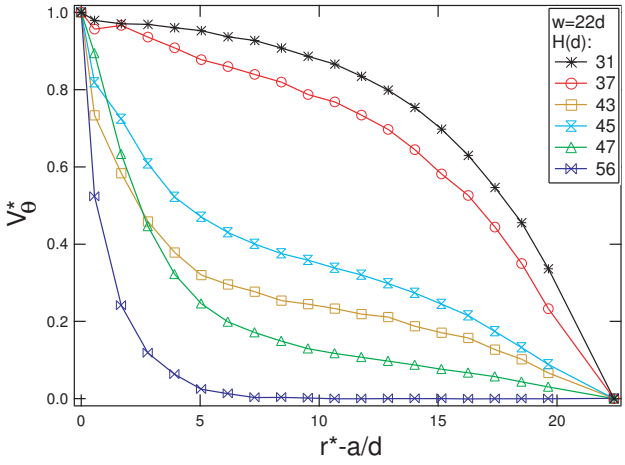

Figure 2.11: Steady state velocity profile for $w = 22d$, or $d = 2mm$. Due to the smaller w/d ratio, $20d$ wide linear region observed in 1mm case cannot exist. Failure tends to occur near the walls.

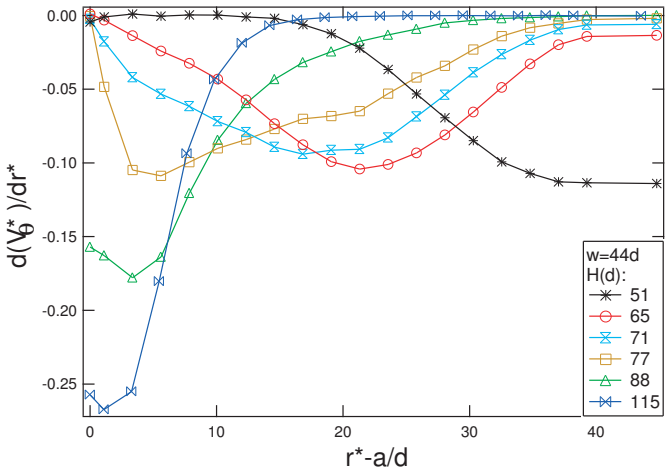

Figure 2.12: Dips in $\frac{dV*_\theta}{dr*}$ indicate the location of shear band for $w = 44d$

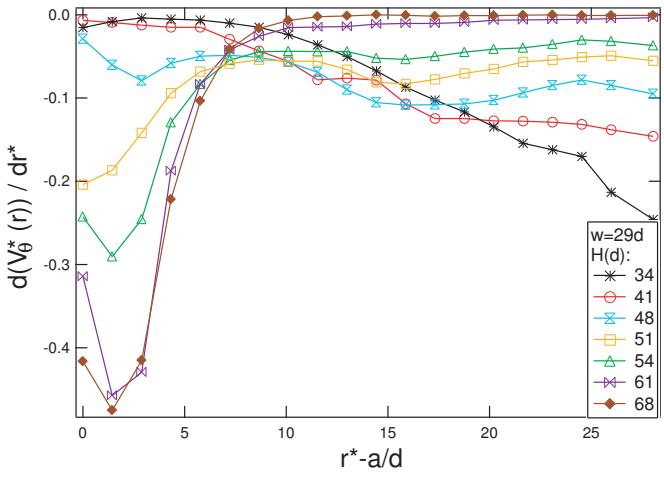

Figure 2.13: Dips in $\frac{dV_\theta^*}{dr^*}$ indicate the location of shear band. For $w = 29d$. Note the secondary dips far from the inner cylinder.

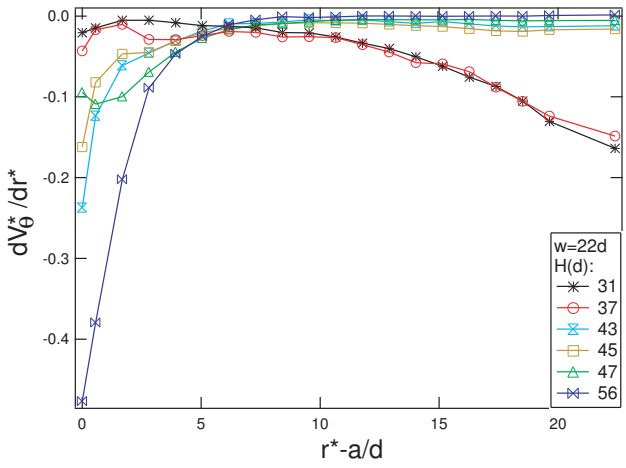

Figure 2.14: Dips in $\frac{dV_\theta^*}{dr^*}$ indicate the location of shear band. For $w = 22d$.

Reasonable fits have been obtained for $w = 44d$ case. Thus the error function,

$$erf(t) = \frac{2}{\sqrt{\pi}} \int_0^t exp(-t^2)dt \tag{2.6}$$

can be used to describe the velocity profiles. The velocity profiles for various filling heights collapse when plotted as a function of a parameter $(r - r_c)/W$, i.e.,

$$V_\theta^*(r) = \frac{1}{2} - \frac{1}{2}erf[(r - r_c/W)] \tag{2.7}$$

This result, shown in Fig. 2.15, is consistent with the results by Fenistein *et al.* in [43]. Significant deviations from the error function fits have been observed for smaller w/d ratios. Fig. 2.16 shows the $w = 29d$ case. In the error function fits presented in [43], w/d was greater than 120. As has been mentioned earlier, the shear zone width of approximately $20d$ has been observed in the $w/d = 44$ case in our system. For smaller w/d, $20d$ wide linear region observed in 1mm case cannot exist. Failure tends to occur near the walls. The resulting velocity profile therefore deviates from the error function shape.

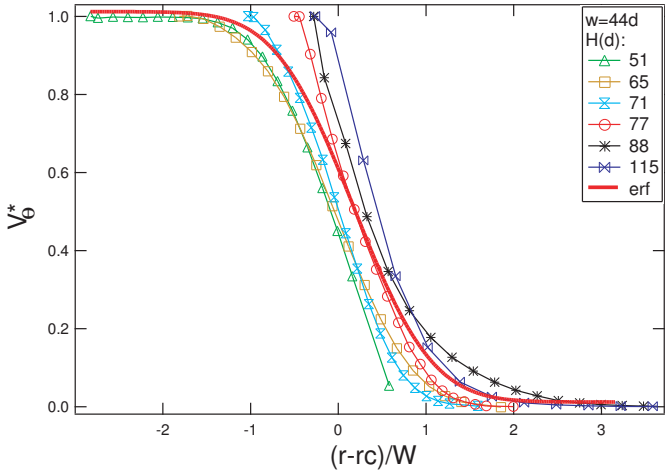

Figure 2.15: Angular velocity profiles for $w = 44d$ scaled by $(r - r_c)/W$ collapse to the error function erf. dV_θ^*/dr^* is first fitted to a gaussian, and the obtained width W and the peak location r_c are used to determine the scaling for each curve.

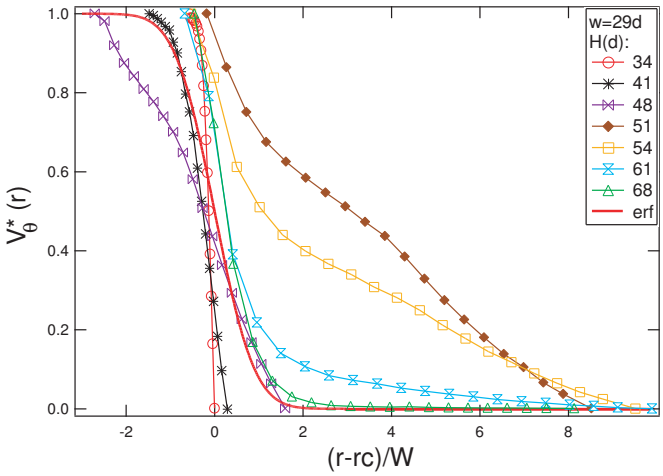

Figure 2.16: The error function fits for $w = 29d$. For smaller w/d, $20d$ wide linear region observed in 1mm case cannot exist. Failure tends to occur near the walls.

2.4.2 Shear Reversals: 90° Change in Principal Stress Axis

As was mentioned in the previous section in Fig. 2.8, transient widening of the shear band occurs upon reversal of shear direction. Our interpretation is that this is due to the shear displacements required to break and re-form the contact network. Since the principal stress points at a 45° angle from the direction of shear (Fig. 2.3), reversing the shear direction results in a 90° change in the principal stress direction. The transiently wider shear band upon reversal of the shear direction means that in regions away from the inner shear surface, the particles move faster and thus gain extra displacements compared to the steady state flow, an indication that the particles must move a certain distance in order to form a new shear band. Thus the extra displacement can serve as a measure of the rearrangements needed to form a new contact network in the orthogonal direction. The extra displacement $l_e(r)$ of particles during this initial transient state is defined by

$$l_e(r) = \int [rV_{\theta(rev)}(r,t) - rV_\theta(r)]dt, \tag{2.8}$$

where $V_\theta(r)$ is the steady state velocity of the particles at a distance r reached after a strain of $\sim 10d$. Fig. 2.17 shows l_e as a function of r. $l_e(r)$ increases with distance from the outer cylinder, except for the layer closest to the inner cylinder surface, which does not show significant extra displacement. Maximum extra displacement occurs at $r \approx 12d$ for $w/d = 44$ and $w/d = 22$. This may indicate that near the shear surface, the contact network is not as preferentially aligned as far from the inner cylinder.

The effects of the breaking and re-forming of the contact network are also ob-

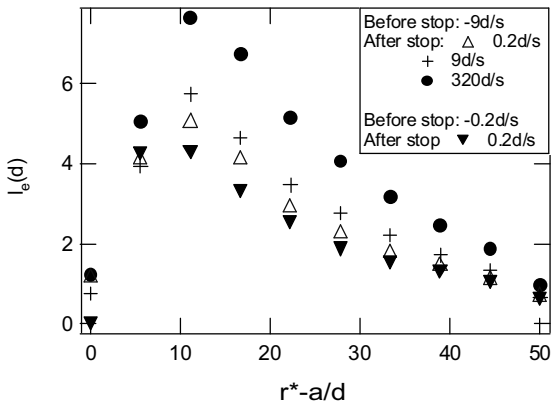

Figure 2.17: Extra displacement $l_e(r)$ as a function of distance r from the shear surface. Compared to steady state shear, particles travel extra displacements due to transiently wider shear band after reversal of shear direction.

served in the strength of the material. Fig. 2.18 shows the evolution of shear torque for stop-start and reversal experiments on the large shear cell as functions of strain represented by the displacement of the inner cylinder. Transient weakening of the shear stress is observed upon reversal. Stress-strain relationship for cohesionless soil (Fig. 2.3c) is known to exhibit similar behavior if the shear direction is reversed during the loading phase. This hysteresis is particularly pronounced in loose soils [40]. In our case, the length scale of the transient phenomenon as a function of particle size is clearly determined, and will be shown later (Fig. 2.23). Similar transient weakening was also found for 2D sheared granular matter without compaction [38] and for sheared particles immersed in a density matched fluid [44].

Material density: If the strength of the material is a function of its density, one might expect that a weaker state should have a lower density. The opposite was observed. Fig. 2.19 shows the height of the material as a function of shear dis-

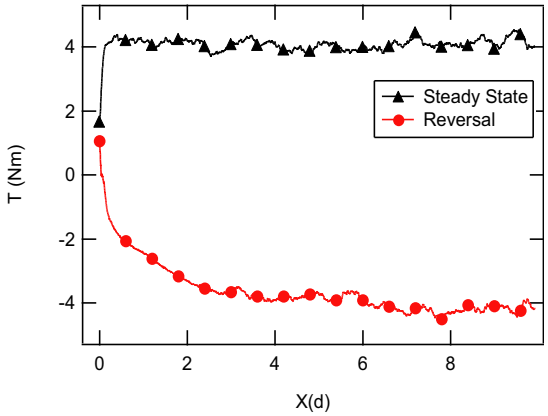

Figure 2.18: Shear stress as a function of shear displacement. When the shear direction is reversed, the shear stress takes 5-10d to reach a steady state. Same direction plot is also shown for comparison. Particle motion on the surface (Fig. 2.8) indicates significantly longer transient period. Different mechanisms are apparently at work for the formation of a stress network and a steady flow.

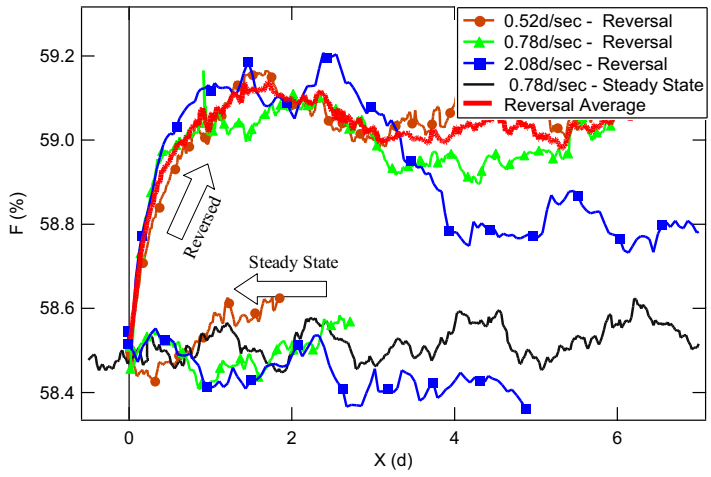

Figure 2.19: Volume fraction F vs. shear displacement X. The material compacts over strain of less than one particle diameter and then gradually dilates again. An exponential fit to the average reversal curves yields a characteristic displacement of 0.4d [8].

placement during stop-start and reversal experiments. The volume fraction remains constant within the experimental error for stop-start experiments. For shear reversal, it increases by 0.5% approximately exponentially over a characteristic shear strain of $0.5d$.

A schematic explanation of these measurements is shown in Fig. 2.20. During steady shear, constant forcing of the particles in one direction forms a contact network. As shown in Fig. 2.3, the principal stress points at a 45° angle from the shearing direction. This network keeps breaking and reforming, but always recovering the overall structure which is responsible for the principal stress direction. The view that the steady shearing state is similar to the initial breaking of a stationary contact network is supported by the observation that the density, shear force, and velocity profile immediately reach steady state values at the start of shear. The shear band is narrow in this case where most stress is carried by a directed force chain network. Reversing the shear direction changes the principal stress direction by 90°, and initially particles are not jammed along the new direction, i.e., no force chain network exists. The shear band is wider, and as shown earlier in this chapter, the material is weaker for this reason. In the absence of a load bearing network to resist shearing, particles are also able to compact slightly under gravity. Gradually particles form a new load bearing contact network to resist the new direction of shear, and a steady state shear is developed.

In the brief period after the initial contact network breaks, the material exhibits fluid-like behavior. Fig. 2.21a and b show velocity profiles during reversal which closely resemble that of a Newtonian fluid. This is another indication that

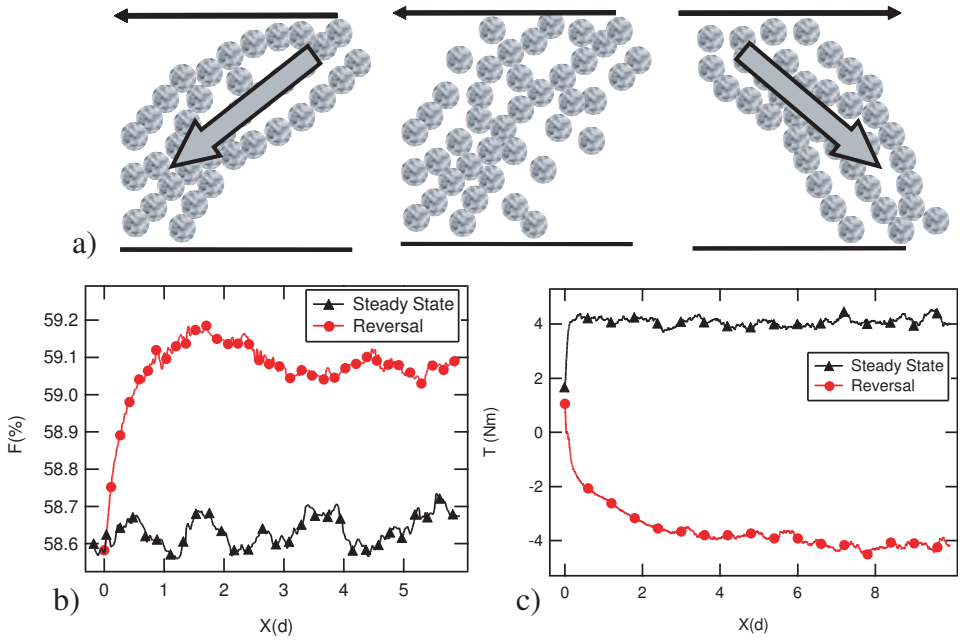

Figure 2.20: The breaking & re-forming of a contact network through shear reversal in dry granular matter in a Taylor-Couette geometry is illustrated schematically in (a), with arrows indicating the principal direction of stress transmission. When shear is started opposite to the prior shear direction, transiently the material compacts and is easy to shear. (b) Column height vs. Strain. Upon shear reversal, the material compacts over a strain of less than one particle diameter and then gradually expands again. (c) Shear torque vs. strain. After shear reversal, shear strain of 3-5 particle diameters is needed to reach a steady state shear force.

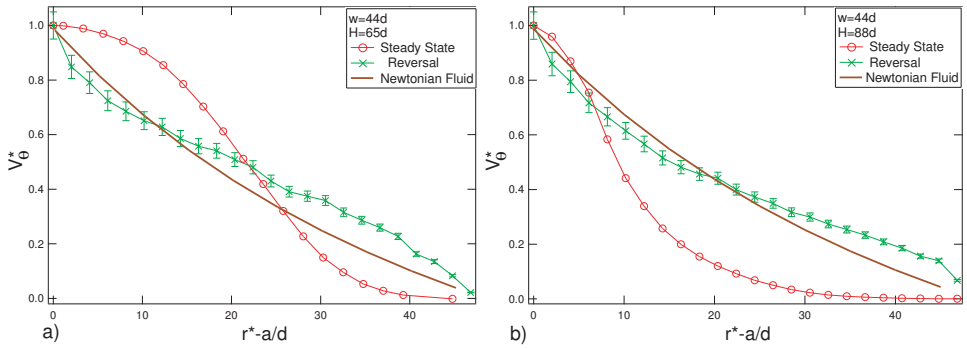

Figure 2.21: Velocity profiles for two different filling heights both exhibit Newtonian fluid-like shape during reversal. Lack of jammed contact network immediately after shear reversal causes material to fail throughout the gap.

the contact network is responsible for some of the unique features of granular materials including the localized shear banding.

Does this surface measurement reflect the flow in the bulk? In order to analyze the 3D structure of grains and shear band widths at various depths in the bulk of the material, a smaller shear cell was used for imaging of the grain interior with a two-photon and confocal microscopy techniques. The granular material used in the small shear cell is highly polydisperse, amorphous silica beads with an average particle diameter of 30 μm. They are immersed in index matching fluid with 0.5wt% laser dye Coumarin152 is added for fluorescence imaging. Shear flow is imaged through the bottom. Figure 2.22a shows a cross section through the granular material about $15d$ into the material. Fig. 2.22b shows a spacetime plot of the intensity of differ-

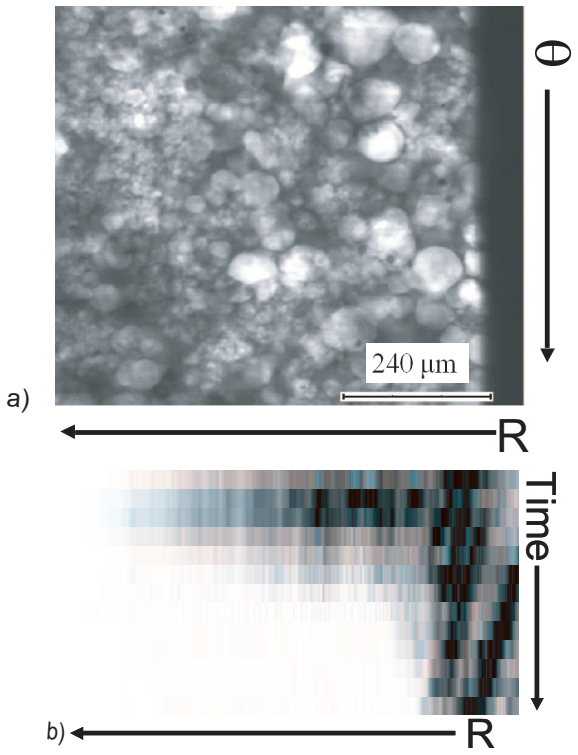

Figure 2.22: Confocal image of the cross section through a granular layer $15d$ inside a granular shear flow (a). Spacetime plot of the θ-averaged intensity of difference images, a measure of the extent of the moving region (b).

ence images, averaged in the θ direction. This is a qualitative indicator of shear band widths. As on the surface, transient widening of the shear band is observed. Significantly more widening of the shear band is observed here, either due to the larger number of layers in the shear cell ($w/d = 170$) or due to the polydispersity of the material used in this experiment. Earlier experiments have also shown that the steady state velocity profiles on the surface and in the bulk are very similar [26].

The anisotropy of the contact network has been seen in constant-density 2D

experiment, where the shear stress and particle contacts are visualized with the use of birefringent disks [41]. Our experiments show that strong *macroscopic* effects result from the anisotropy, i.e., compaction and weakening, which are observable during the onset of shear flow. These effects provide an indirect measure of the anisotropy of the configuration of a granular assembly under shear stress. In our 3D system, the characteristic strain over which the system compacts indicates that particles need to move by up to $1d$ to "break" the network of particle contacts. The extra displacement of particles, and the associated lower shear stress indicate that each layer of particles may move an extra distance relative to the layer farther from the shear surface before the network reforms. Repeated reversals of the shear direction result in further compaction of the bulk, as we will discuss in Chapter 5.

2.4.3 Scaling Issues: Particle Size and System Size

Shear displacement of the inner cylinder is responsible for the jamming, breaking, and re-jamming of the granular contacts that we have observed in the previous section. Then, what determines the shear displacement over which the breaking and re-forming of the granular contact network take place? In order to investigate the role of the particle and system sizes, we have repeated the measurements with mixtures of different particle sizes. The formation and stabilization of shear bands as indicated by the extra displacements scale with w/d, where w and d are the shear cell width and particle diameter, respectively. Fig. 2.23 shows the development of torque after shear reversals in the large shear cell, plotted against the displacement

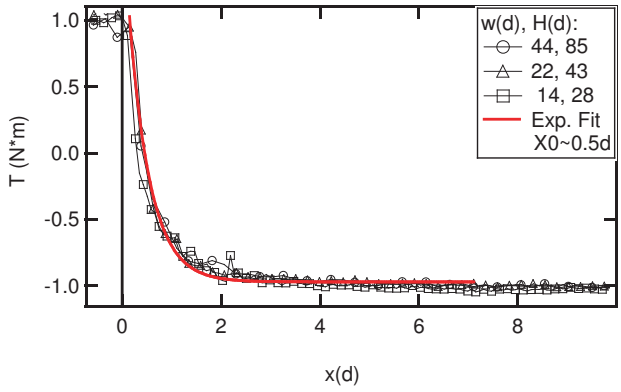

Figure 2.23: Torque exerted by the inner cylinder upon reversal of shear direction is plotted against shear displacement, x. Curves for $w = 44d$, $22d$, and $14d$ all collapse onto each other when the torque is normalized by peak to peak value, and plotted as a function of shear displacement in units of particle diameter d. Collapsing curves suggest that the development of a contact network scales with particle diameter. An exponential fit yields a characteristic displacement of 0.5d.

of the inner cylinder in particle diameters. Transient weakening of the shear stress is observed upon reversal, with gradual recovery to a steady state. When shear is started in the same direction after a pause, the system reaches a steady state shear stress in less than 1d, as shown in Fig. 2.18. Curves for w=44d, 22d, and 14d all collapse onto each other when the torque is normalized by peak to peak value, and plotted as a function of shear displacement, x, in units of particle diameter d. Collapsing curves suggest that the development of contact network scales with particle diameter. The characteristic displacement, $x_0 \approx 0.5d$ of the torque development is obtained by a fit to an exponential function of the form $T = A + exp^{x/x_0}$.

Figure 2.24 shows the extra displacements due to shear reversals as a function of distance from the inner cylinder. Note that the extra displacements increase roughly linearly away from the stationary outer cylinder. This indicates a linear

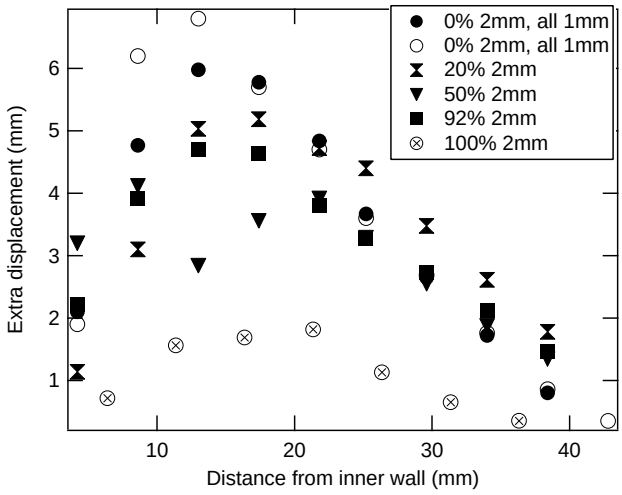

Figure 2.24: Extra displacement as a function of distance from the inner cylinder. The extra displacement is a measure of the integral under the peak in the velocity curves introduced in Fig. 2.17.

strain that is superimposed on the steady state shear flow.

The superimposed strain is large (up to 22%) relative to the free strain one might expect if each radial granular layer in the system were to shift with respect to the nearest layer. One indication that the linear strain is not due to layer by layer rearrangements of grains comes from the dependence of this extra strain on particle size. We measured the extra strain for 1mm and 2mm particles, and for a range of mixtures of particle sizes, as shown in Figure 2.25.

We find that the linear strain decreases as the number of particles needed to bridge the shear cell gap decreases. Therefore the free strain cannot be due to local rearrangements of layers of grains, but must be related to cooperative rearrangements as the system develops a new contact and force network.

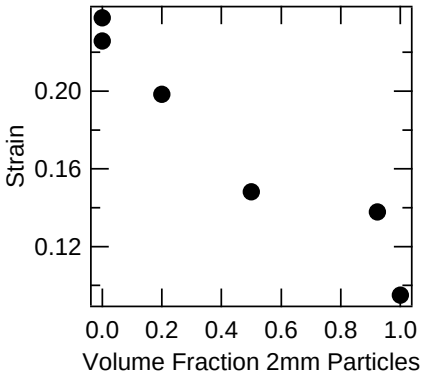

Figure 2.25: Additional linear strain (expressed in units of extra displacement/inner cylinder displacement as a function of the fraction of large (2mm) vs 1mm particles. The linear strain is larger for smaller particles.

2.4.4 Shear Band Location and Convection

The radial velocity profiles are shown in Fig. 2.26. The absence of radial velocity in steady state shear is reported in [43]. We have seen, however, that velocity in the radial direction (V_r) has a dip near the center of the shear band. When the filling height is large enough, i.e., the effect of the bottom plate is negligible on the top surface, it is possible that a convection roll is centered around the shear band.

Gaussian fits have been performed to determine the dip locations of $\frac{dV_\theta}{dr}$ and V_r, and plotted on Fig. 2.28. Coinciding peak positions are apparent. Note that the crossover at $H = 75$ coincides with the switch of the shear band from the outer to the inner wall. although there is no clear explanation for the cross over at $d = 75$.

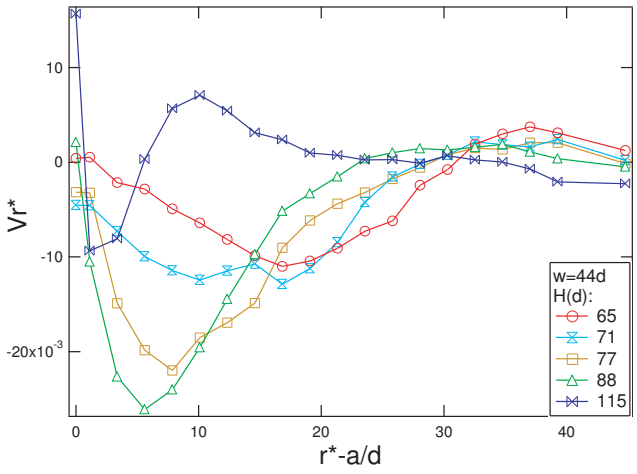

Figure 2.26: Steady-state V_r^* for 1mm particles. Negative values indicate that the radial velocity points toward the inner wall. Locations of minima move closer to the inner wall for greater filling height. $V_r^* = V_r/\omega a$, and $r^* = r/d$, where d is a particle diameter.

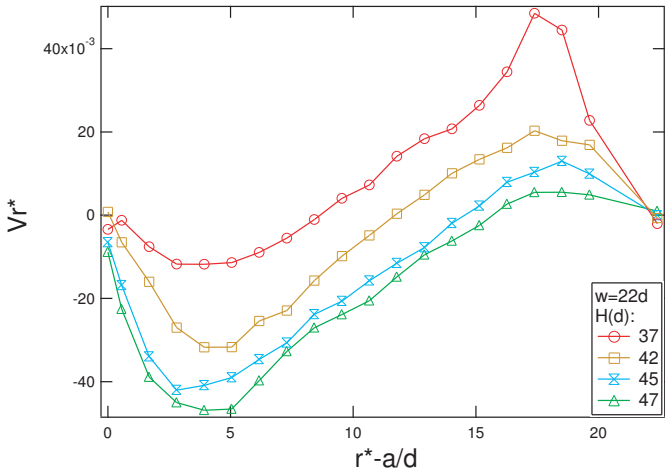

Figure 2.27: Steady-state V_r for 2mm particles.

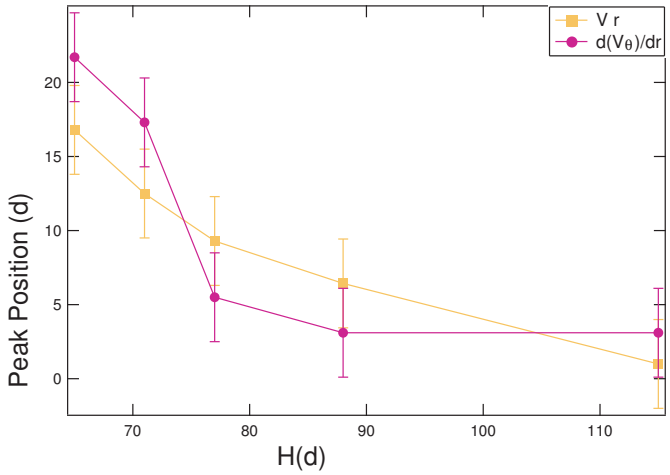

Figure 2.28: Minima of V_r^* tend to occur near the minima of $\frac{dV_\theta^*}{dr^*}$, suggesting the presence of a convection role centered around the shear band. In this convection roll, particles travel toward the center on the top surface, downward where $r^* < R_c$, outward near the bottom, and upward where $r^* > R_c$, where R_c is the radius at which a maximum in the absolute value of $\frac{dV_\theta^*}{dr^*}$ occurs.

2.5 Chapter Conclusions

In this chapter we reviewed the memory effect of sheared glass spheres in a Taylor-Couette cell. Widening of shearband, weakening of shear forces, and compaction have been observed upon shear reversal. We have also shown that steady state shear banding can be tuned by varying the particle to system size ratio, in addition to the already known tuning by varying the filling height of the material. We find that the direction of prior shear influences how granular matter starts to flow. If shear flow is started in the same direction as prior shear, the system reaches a steady state flow with minimal strain of less than one particle diameter. If the shear direction is reversed, the material compacts by a fraction of a particle diameter over a characteristic strain of $0.5d$, an indication of the breaking of the load

bearing contact network. Also upon reversal, material far from the shear surface flows significantly more than in the steady state, and the shear stress is reduced, both over a characteristic strain of $5 - 10d$. We conjecture that the main cause of history dependence is the stress chain network which transmits forces in granular media. Stress transmission in granular media are known to depend strongly on how the systems are jammed. For example, the force at the base of a pile of grains has a maximum in the center of the pile if the grains are dropped from a sieve, but has a maximum in a ring around the center if the grains are dropped from a single opening above the center [45]. In two dimensional model systems, two very different stress chain networks were visualized directly [7] (Fig. 2.5b). DEM simulation of box-shear test (Fig. 2.3) clearly shows the stress chains preferential in the direction of shear [6]. Mixtures of 1mm and 2mm particles produced results which fit between 1mm and 2mm data.

Chapter 3

Flows due to Local Forcing - Penetrometer Testing

3.1 Chapter Overview

In this chapter we focus on local rearrangements of granular matter due to local forcing. We explore the failure of the contact network by direct observation of 3D particle rearrangement due to penetration of a solid rod through a granular medium. The strain transmission spreads around the rod in a ring like manner with greater rearrangement farther away from the rod than directly under the rod. Materials compacted by compression from the side fail farthest along the pre-formed stress chains. The relevance of rod penetration experiments to soil mechanics and engineering applications, and connection to the force measurements results will be discussed.

3.2 Background Information

Much of soil mechanics is based upon vast amounts of empirical data from controlled experiments on model soils and field observations. Models based on these data do a reasonable job of predicting the yield strength and the flow properties of soil [39, 46]. These results indicate that the yield strength and flow of soil are reproducible, and behavior can be extrapolated to some degree. However, despite

much effort, the equations describing the yield strength and flow of soils, or even equations for the arguably simpler case of dry spherical grains remain empirical [47]. Empirical equations require validation through thorough data gathering before their applicability can be established. Fundamental understanding of granular flows based on their microscopic origins will be helpful toward building a model with more predictive power. For example, construction of a structure on the Lunar or Martian surface, be it a habitat for humans or a landing site, requires proper evaluation of the strength of that surface. Very limited on-site evaluation is possible, and the evaluation method needs to be simple and robust. Among numerous experiments performed on the Moon, standard penetrometer testing has been carried out on the lunar surface [48]. Interpreting the data is challenging since it relies on the empirical models, with only very limited data and soil samples from the Moon, and no soil samples from Mars available to test whether the models are still applicable under lunar or martian conditions. In particular it is unclear whether the existing models can be extrapolated to completely dry materials in reduced gravity. In this chapter we propose two new experimental approaches to improve our understanding of how granular matter flows when subjected to penetrometer testing. These techniques allow for direct imaging of 3D fields of particle rearrangement and simultaneous force measurements.

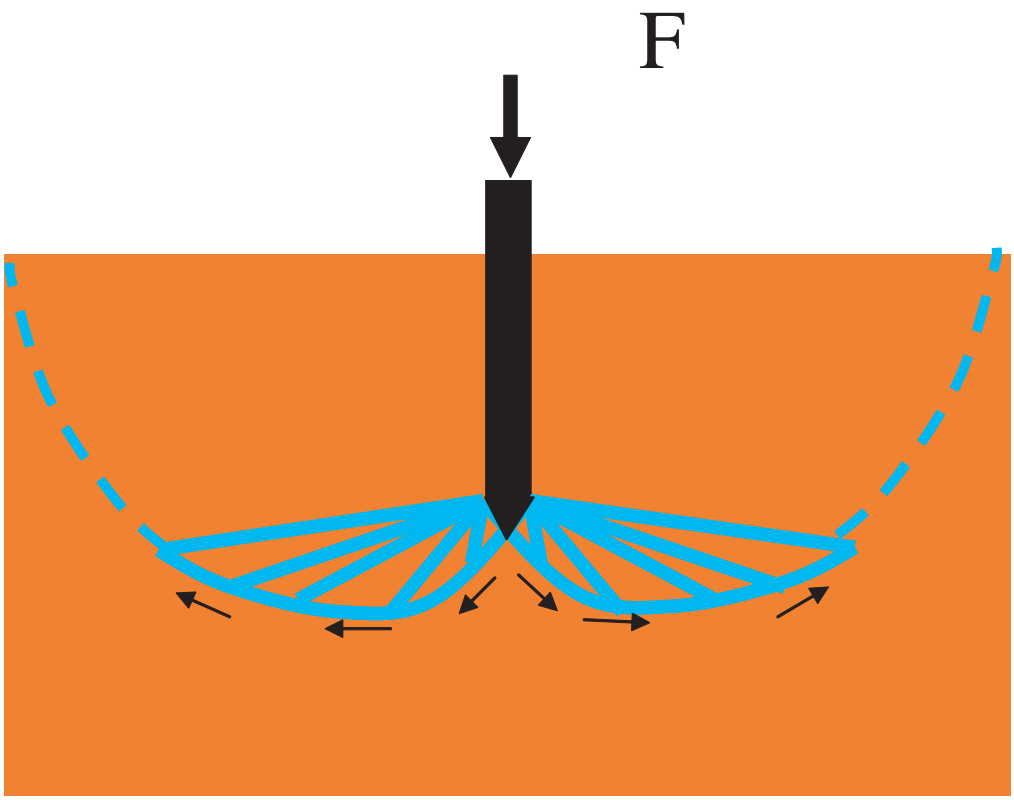

Figure 3.1: Schematic of the shape of a typical failure surface of soil found in bearing capacity calculations. Calculations of forces rely on this assumed shape of the flow field.

3.3 Experimental Background

Cone penetration testing (CPT) is a standard method for evaluation of soil strength for construction purposes, in which a rod with a conical tip is inserted into the ground for measurement of resistive forces, pore pressure, etc. Classic theories in soil mechanics such as the bearing capacity and cavity expansion theories offer possible mechanisms, while the motion of soil particles can explain the measured forces on the penetrometer [49, 50]. With a sufficient number of fitting parameters these theories offer reasonable predictability of soil strength. For example, a typical shape of the failure surface is illustrated in Fig. 3.1. Here the material is assumed to fail along the curved lines, and from the density and cohesive properties of the soil the amount of force required to slide the material along the slip lines is calculated. Although in reality the deformation of the soil occurs not along a single slip but throughout the bulk of the material, this model has been used extensively in the past.

3.3.1 Failure of Granular Contact Network

How a granular material fails depends on the sample preparation and direction of prior forcing, as we have noted in the previous chapter. 2D experiments on birefringent disks have shown recently that isotropic compression leads to a densely branched network of stress chains, while pure shear with one compressive and one expanding direction leads to an anisotropic network of stress chains that is aligned with the compressive direction [7]. In a system jammed by shear, the direction of

forcing relative to the preferred direction of stress chains strongly influences how the material will start to flow, and influences the forces at the start of the flow. As presented in chapter 2, if the material is sheared in the direction of force chains, a local shear band forms almost instantaneously when the material starts to flow. If the material is sheared with a principal stress axis perpendicular to the force chains, e.g., if the direction of shear is reversed as shown in Fig. 2.20a, all particles initially move and the initial shear strength of the material is significantly smaller [8]. Without load in the direction of the existing force chain network, the material can actually compact as shown in Fig. 2.20b while the shear force is smaller, i.e., transiently form a denser, weaker system. The steady state shear force is recovered after a shear displacement of 3-5d. A qualitatively similar, but quantitatively smaller effect was found in two dimensional model systems [51].

One possible limit of validity of bearing capacity theory is how well it predicts flow fields in anisotropically stressed granular matter. The theory does not take into account the possibility of anisotropic force transmission. As has been shown, for granular material sheared in a Couette cell the prior history of shear, which leads to anisotropic, force transmitting grain contacts, strongly influences how granular matter starts to flow [8]. Evidence that the direction of prior shear influences the subsequent flow has also been reported in geological granular flows [2]. While the theories relate experimentally observed stresses to assumed failure planes and flow fields, only limited direct information is available on these flow fields. More detailed observations of the true failure planes and flow fields should help validate the theories and point out limits of applicability. These results indicate that the memory effect

of the load bearing contact networks of grains influences how the granular material will start to flow. Thus we expect that memory effects will appear in both the strength of the granular material and the flow of grains when localized failure of the contact network is initiated through the penetrometer testing.

In penetrometer testing the rod tip continuously moves through new regions of the sample and initiates a localized flow near the tip. Many grains only flow over short distances, without reaching a steady flowing state. Thus we expect that the dependence on the prior shear history of the sample would not just be at the start of penetrometer testing, but throughout the procedure as new regions of the granular pile are continuously penetrated. Another possible limit of validity is near boundaries. Boundaries influence the force on the penetrating tip, and generally experiments are carried out far from boundaries for cone penetrometer testing. However, sometimes the cone penetrometer may encounter an unexpected obstacle. As we have seen in Chapter 2, however, flow fields change qualitatively in confined geometries. Therefore a large obstacle placed near the penetrometer should affect the force on the unit. Past attempts to directly image the soil movement during CPT have been limited to a quasi 3D geometry in which a penetrometer in the shape of a half cylinder, pressed against a glass side window, was lowered into a real soil sample as illustrated in [49].

3.3.2 Role of Confining Walls in Granular Contact Network

Stress pattern shown in Fig. 2.5 indicates that the stress chains formed by a vertical point force are redirected horizontally toward the side walls. This is one of the features unique to granular materials which deserves more exploration.

The following approach was first proposed by Janssen and later developed by Lord Rayleigh. The pressure of an ordinary fluid standing in a cylinder, for example, can be written as $p = \rho gh$. In granular case we must take into account the fact that some of the vertical load is redirected to the side walls. Let us consider a cylindrical container of radius r. Here ρ is the bulk density of granular material. K is a the coefficient of redirection. A sidewall of area $2\pi rdh$ supports the redirected pressure. μ is the static coefficient of friction. Then the equilibrium equation is

$$\pi r^2 dp + K\mu 2\pi rpdh = \rho g\pi r^2 dh, \tag{3.1}$$

which has a solution,

$$p = \frac{\rho gr}{2K\mu}\left[1 - exp\left(\frac{-2K\mu}{r}h\right)\right]. \tag{3.2}$$

The value of K is of order 0.5 and dependent on the arrangement and properties of grains. Near the top surface $p = \rho gh$ still gives a good approximation, but the pressure quickly saturates to an asymptotic value of $p = \frac{\rho gr}{2K\mu}$ for greater depths. The pressure in the container to approach a constant value roughly at the depth of r with $\mu = 1$. A more detailed analysis can be found in [52].

3.3.3 Penetrometer Experiments with Spherical Grains

Detailed studies of the influence of boundaries were carried out by the Schiffer group [53, 54]. The studies focused on the effect of nearby obstacles on the penetration force. Note that the authors designed a special filling procedure to create reproducible initial conditions, since the results were sensitive to the preparation history of the sample. When the penetrometer is lowered into the material, an exponential rise in the force is observed near a buried obstacle. The rise is preceded by a decrease in the force if the walls of the obstacle are smooth. The characteristic length λ over which wall effects are measured, and it exhibits the scaling of $\lambda \propto \sqrt{F_0/r}$, where F_0 is the penetration force at the same depth in the absence of a boundary, and r is the radius of the penetrometer tip. This scaling is not yet dimensionally correct, and it is not yet clear how the length λ depends on other parameters such as gravity.

The aim here is to develop the tools to carry out a microscopic validation of bearing capacity theory, and to study the role of stress anisotropies and boundaries on the particle motion during penetrometer testing. This requires (1) soil material which allows imaging of the interior of the bulk, (2) imaging techniques with subparticle resolution, and (3)computer algorithms to track the motion of individual particles. Recently, transparent soil simulant consisting of particles in an index matched fluid has been introduced (described below). This has allowed progress toward imaging vertical cross sections of transparent soil illuminated by a laser sheet. Flow in these cross sections has been analyzed by digital image correlation

[55].

The imaging has mostly relied on following the motion of tagged particles. Since in a penetrometer motion is highly localized we expect that significant information about the physics of rearrangement events is contained in local correlations in particle positions and displacements. Thus tagged particle motion does not yield a complete picture. In particular, complete volume scans are necessary to study how the prior history of the sample influences the failure of a jammed granular material.

We use two imaging techniques (1) confocal and two-photon laser scanning microscopy and (2) laser sheet scanning. Polydisperse, non-spherical particles and spherical particles are used. Our tools have enough resolution to make possible the full 3D analysis of material flux during CPT. Extraction of the position and displacement of individual particles is possible with the latter method.

3.4 Confocal Imaging of Deformation Fields: Transparent Soil and Spherical Particles.

3.4.1 Sample Preparation

The granular material used in this experiment consists of irregularly shaped amorphous silica particles (Flo-Gard SP, manufactured by PPG Industries). Rheological properties of this material are extensively studied and published in the civil engineering and geotechnical literature [56, 57]. This material, when immersed in fluid, is considered a transparent soil model for clay. Our observations of particle sizes are consistent with the published particle size range of 2 to 150 microns, with

an average size of 30 microns. Cargille Laboratory's Code S1050 oil (n=1.447) is used as the index-matching fluid. To produce a transparent mixture of particles and index-matching oil suitable for two-photon laser scanning microscopy, the oil is first mixed with laser dye Coumarin 152 at 0.7% by weight. Particles and oil are mixed together in a vacuum chamber at or below $200mmHg$ to eliminate the possibility of air bubbles entering the mixture. Alterntatively, the same oil and fluorescent dye iodoacetimide tetramethylrhodamine (IATR) have also been used with similar results. For all materials mixing in near-vacuum was found to be a faster and more reliable method to prevent trapped air bubbles than mixing under atmospheric pressure first and then de-airing. Absence of bubbles is essential for maintaining the transparency of this otherwise indexmatched medium.

3.4.2 Experimental Results - Confocal Microscopy

The general setup is depicted in Fig. 3.2. Granular material immersed in index matching oil is placed in a square glass container (25mm $\times$ 25mm $\times$ 25mm). The container was filled with particle/oil mixture up to a height of 10mm. The material was then slowly stirred and overturned for isotropic initial arrangement of particles, and allowed to settle for several hours. A steel rod (0.79mm diam.), which serves as a penetrometer, is attached to a steel leaf spring. Deflection of the spring due to resistive forces in the granular medium is measured by an inductive displacement sensor mounted above the spring. The spring deflection provides a measure of the force needed to penetrate the granular medium. A vertical translation stage controls

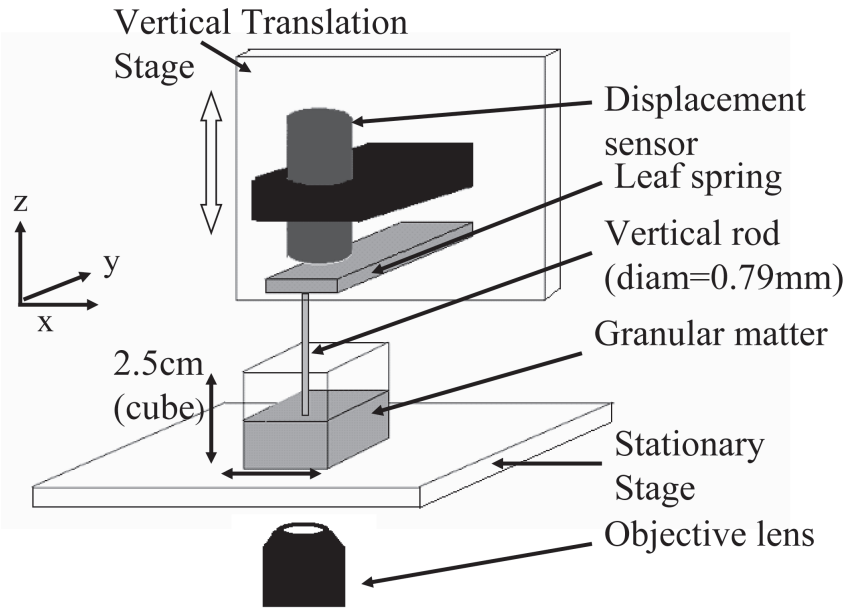

Figure 3.2: Schematic of the penetrometer setup for confocal microscopy

the position and speed of the penetrometer assembly. Although the container size to grain size ratio has been found to play a role in the response characteristics of the material, the setup described above exceeds the ratio of container size to particle size of 40, beyond which no observable effects of the container have been seen [58]. A Leica IRBE laser scanning microscope was used for imaging an area of 4.75mm $\times$ 4.75mm centered around the rod. 500 x-y cross sections were imaged from the bottom boundary up to a height of 2.5mm.

Difference images obtained from sets of images taken before and after a penetrometer displacement of 200 microns show particle movement as black and white, and stationary regions as gray. From the stacked difference images of x-y sections we reconstructed y-z and x-z sections to illustrate the shape of the shear zone as shown in Fig. 3.3. The rod tip shown in the figure is at approximately 8mm from

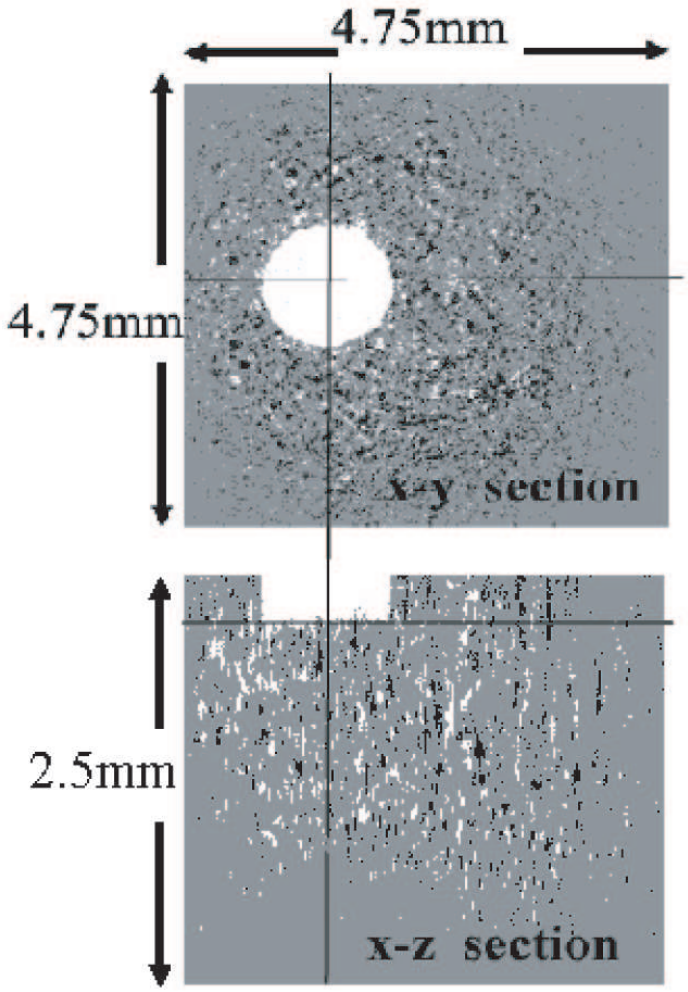

Figure 3.3: Difference images showing the shape of displacement field created by the penetrometer.

the top boundary and 2mm from the bottom. The shear zone spreads in a ring-like shape around the penetrometer. The x-z section reveals the shape of the shear zone. Black and white spots adjacent to each other indicate motion of particles or particle aggregates from black to white. The shape of the zone where particles move is in qualitative agreement with the shape expected from bearing capacity theory. Note that our experiments used a flat tip rather than a cone shaped penetrometer tip, so a direct quantitative comparison is not possible. Grey areas indicate no observable particle motion. As a more quantitative measure of the shear zone shape, the area density of bright pixels as a function of radial distance from the rod center is shown in Fig. 3.4. Deformation is more pronounced on the side of the rod than directly under it.

How do the observed motion relate to the stress distribution? One might assume that larger deformation is an indication of larger stress prior to flow. In two dimensions, the stress response of the contact network to a point force has been directly imaged in an assembly of birefringent disks [36]. Ordered assemblies of monodisperse and bidisperse disks showed stress peaks on either side of the point force, broadening with increasing depth. When pentagonal particles were used for "disordered" packing, the peak stress was found below the point force.

In the second experiment we studied a system compressed from the side, which leads to a stress chain network roughly perpendicular to the penetration direction (if one extrapolates the 2D observations on the topology of the stress chain network described in section 2.1 to three dimensions). Internal imaging of the motion of such anisotropically loaded samples under rod forcing shows that particles have a larger

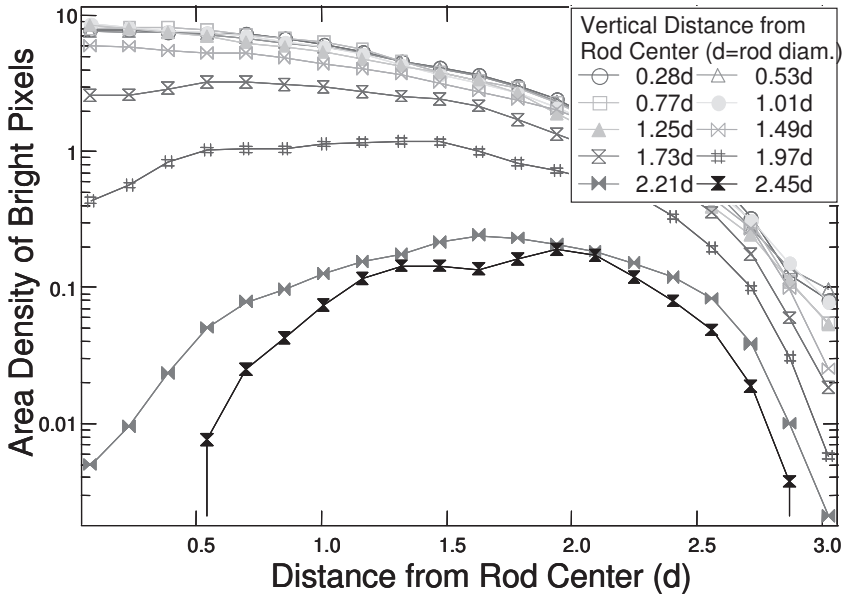

Figure 3.4: Normalized number of bright pixels from the difference images as a function of horizontal distance from rod center. For greater vertical distance from the rod particle motion is restricted directly under the rod.

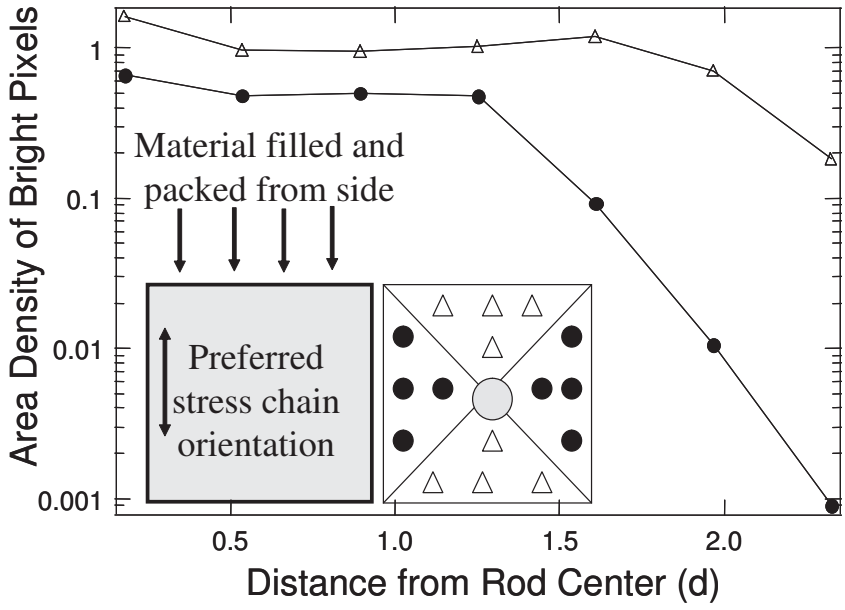

Figure 3.5: Normalized number of bright pixels from the difference images for anisotropically loaded material. Particle motion is observed predominantly along the preformed stress chain network, particularly for greater horizontal distances from rod center.

tendency to move if they are positioned in the direction of the force chain network than when they are perpendicular to it. This effect is particularly pronounced for particles far from the rod center as shown in Fig. 3.5. We are currently collecting systematic data to confirm these initial observations that the stress chain network direction and the location of particle motion are correlated. Difference images do not yield information about the direction of motion, so it is not clear whether particles move parallel or perpendicular to the direction of stress chains.

3.5 Laser Sheet Scanning of Spherical Particles

Granular materials consisting of spherical particles have been extensively studied both numerically and experimentally. Their behavior has been explored in various geometries such as inside rotating drums [59, 60] and avalanches on slopes [61], where direct experimental observation of the interior is often impossible. There have been observations of fluid immersed spherical particles in a cylindrical Couette cell, in which a thin sheet of laser illuminates a cross section of the interior [42]. The 3D imaging technique presented in this section uses a laser sheet(Stocker-Yale Lasiris 35mW, 635nm) and transparent spherical glass particles (Glen Mills, $d = 3mm$) immersed in Type DF immersion oil by Cargille Labs at a concentratio of0.0004% by weight. The dye was first dissolved in a small quantity of acetone and then added to the oil to avoid clumping. The setup is shown in Fig. 3.6a. When the laser sheet passes through a mixture of dyed fluid and particles, it causes fluorescence in the dyed fluid. Particles appear as dark circles with varying diameters depending on their positions relative to the laser sheet. A high sensitivity, high resolution camera (Sensicam) mounted perpendicular to the laser sheet records the cross sectional images. We have chosen a lens such that one particle diameter corresponds to 20 pixels on the captured image. The camera and the laser sheet are moved across the sample with a translation stage in steps of a fraction of a particle diameter.

Images obtained this way are x-z cross sections, spaced in y-direction by $0.1mm$. Images are first inverted so that the particles appear as bright circles, and particle tracking code in IDL was used. The algorithm identifies the center (x

and z coordinates) of the bright circle in an image. Since the particle is spherical, the x-z coordinates of a given particle do not change from frame to frame. The same particle to appear at the same x-z coordinates in the next frame. Since the particle is $3mm$ in diameter, this should continue for approximately 30 frames. A typical image at this point in analysis is shown in Fig. 3.6 (b) and (c). The average frame number is then used to calculate the y-coordinate of the center. The process is performed for every identified particle in the images, and coordinates of each are tabulated.

Forces acting on a sphere of mass m and radius r freely sinking in a fluid with viscosity η can be written approximately as

$$F = m\frac{dv}{dt} = \frac{4}{3}\pi r^3(\rho_{glass} - \rho_{oil})g - 6\pi\eta_k r v, \tag{3.3}$$

which gives a terminal velocity of

$$v_{terminal} = 2r^2(\rho_g - \rho_o)/\eta_k \approx 10^{-1} m/s. \tag{3.4}$$

In order to avoid the influence of viscous drag on the particles, rod manipulation speed was limited to $10^{-4} m/s$. In this regime, viscous drag on the particles that move at rod speed is approximately three orders of magnitude less than the gravitational force acting on the particle. One may find the Reynolds number of such a particle traveling at the terminal speed, $R_e = vL/\eta_k \approx 10^{-1}$, as another way to illustrate the velocity regime in which experiments in this section are performed.

In first studies we have used this system to image rearrangements due to a penetrometer. In order to observe the effects of pre-formed stress chains on the motion of spherical particles, a laser sheet was kept at a fixed height while the rod

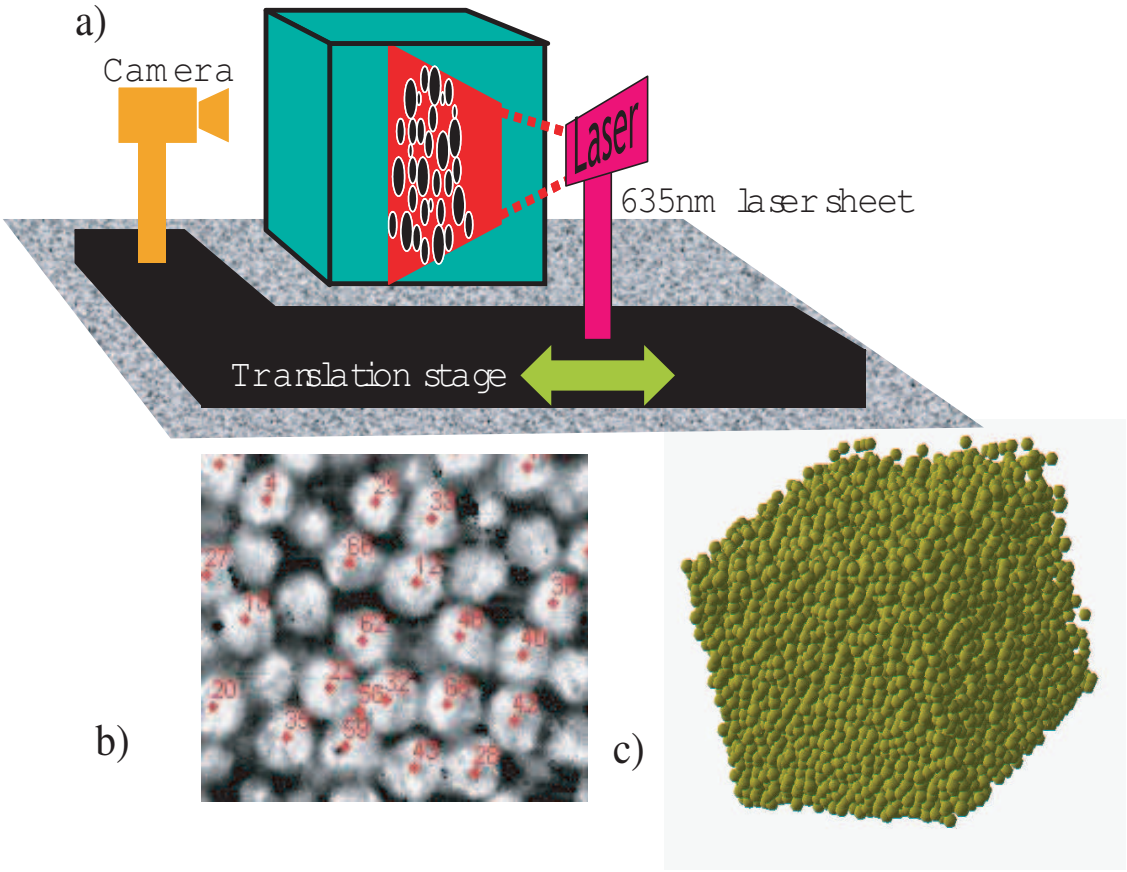

Figure 3.6: Direct imaging of 3D jammed granular material using laser sheet scanning: Glass spheres embedded in dyed, index matching oil are illuminated with a laser sheet as shown in (a). In (b), center positions of particles are identified and tracked in a cross sectional image. (c) shows the particle positions in 3D reconstructed from the 2D cross sections.

was lowered into the mixture. Analysis shows that particles move faster and farther along the direction of compression, similar to the result from the irregularly shaped particles as shown in Fig. 3.5.

3.6 Summary

The use of penetrometer type soil testing in new environments such as Moon or Mars will require extrapolation of bearing capacity theories toward different gravity levels and vastly different environments and materials. Hence, it is important to thoroughly test the limits of applicability of bearing capacity theories.

Here we demonstrated 3D imaging of particle rearrangements inside granular matter using two complementary methods. We use "'transparent soil"', rough silica particles of a range of sizes that are immersed in an index matching fluid. The system is imaged in 3D with a confocal microscope. The displacement fields are qualitatively similar to predictions from bearing capacity theory.

The data also indicate that the direction of prior shear is correlated with the location of where particles move away from the rod. Direct laser scanning works on spherical model system and allows for detailed studies of the role of the boundaries and stress anisotropies, but is less well suited to compare to bearing capacity theory since it does not allow the same number of particles, or the odd shape of particles used in confocal microscopy.

Chapter 4

Vibration, Temperature and Shear Induced Compaction

4.1 Chapter Overview

Granular materials are known to achieve higher packing fraction when subjected to mechanical vibrations. In fact, vibration-induced compaction has been extensively studied the past [23, 62, 63, 9]. In vibration-induced compaction, the packing fraction increases quickly in the beginning, then gradually approaches an asymptotic value. In collaboration with a research group at Universite de Rennes I, a new type of granular rearrangement event was discovered in confocal microscopy of vibrated oil-immersed granular material [9]. Aside from the well known cage motion in which a particle is surrounded by the same neighbors, a rare rearrangement events occur in which a grain moves significantly more relative to others. Though rare, such "jumps" are shown to play an important role in the evolution of packing fraction.

Temperature variations cause the grains and confining boundaries to expand and contract. When a granular packing in a container is heated and cooled repeatedly, the process usually yields results similar to tapping [22, 64]. Expanding and contracting the particles or the container cause the material to compact and achieve a higher packing fraction. Preliminary results shared by the Schiffer group at Penn State University indicate that the compaction is a highly reproducible function of

temperature and number of cycling. As has been seen so far, the response of the granular material depends strongly on the way the grains are put together to form the bulk. Compaction of granular material can be seen as relaxation and aging of contact network, in which the cage motion of grains results in more efficient packing. Glass transitions of liquids are thought to consist of formation of cages and their rearrangements For this reason granular systems provide a convenient model for glasses. In commercial grain storage, the daily and seasonal variations in ambient temperature cause the grain container to expand and contract, causing rearrangements of grains inside. Consideration of temperature induced compaction of soil may also be necessary on Moon or Mars. Direct observation of local scale particle rearrangement is crucial to the understanding of the evolution of packing fraction. Microscopic mechanisms of compaction due to temperature cycling, however, have not been extensively investigated in the past. In this chapter, compaction of granular packing is realized by using containers which have different thermal expansion coefficient than that of grains. Oil immersed grains are observed by the laser sheet scanning unit introduced in chapter 3.

4.2 Experimental Setup for Vibration-Induced Compaction

A schematic of vibration induced compaction experiment is shown in Fig. 4.1 Glass cylinder ($d = 6mm$) contains a mixture of spherical grains ($d = 0.6mm$) and index matching oil (Cargille Labs). The sample is subjected to mechanical vibration so that the the bottom layer of particles leave the cylinder bottom during a single

oscillation. Cross sectional images are obtained by the confocal microscope, whose objective is placed under the cylinder. Accelerometer attached to the actuator monitors the shaking acceleration.

4.3 Experimental Setup for Temperature Cycling Experiment

The temperature cycling setup is pictured in Fig. 4.2. A cylinder made of polymethylpentene, 5cm in diameter, contains 3mm glass beads and dyed oil mixture introduced in Chapter 3. The cylinder is immersed in a water tank. The thermal expansion coefficient of polymethylpentene is $1.17 \times 10^{-4} K^{-1}$, and that of glass is $0.9 \times 10^{-5} K^{-1}$. Therefore the variation in temperature mainly causes the cylinder to expand and contract. The temperature of the cylinder and its contents is varied by changing the temperature of the surrounding water. A separate measurement is performed to confirm that uniform temperature of the sample is achieved after 45 minutes. Laser sheet sweeps across the sample, illuminating the dyed oil. Images are taken from the above. Particles and container match the materials used in ongoing systematic studies by the Schiffer group at Penn State University.

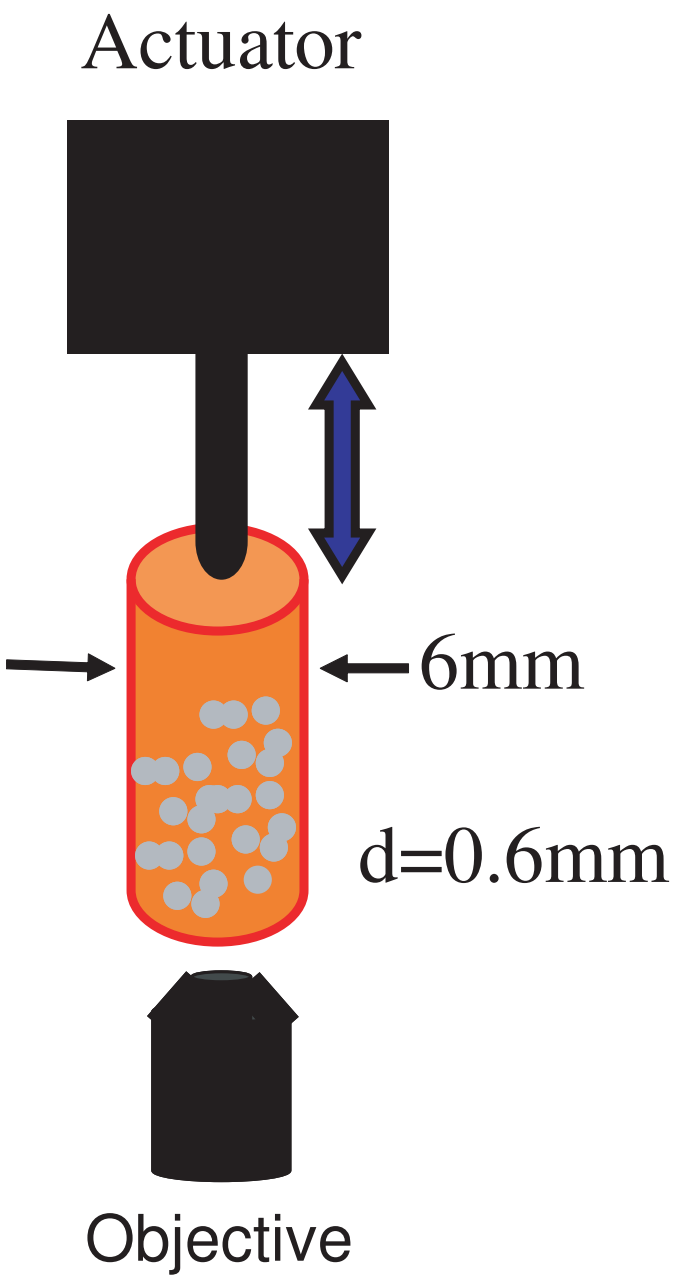

Figure 4.1: Confocal microscopy of vibration induced compaction.

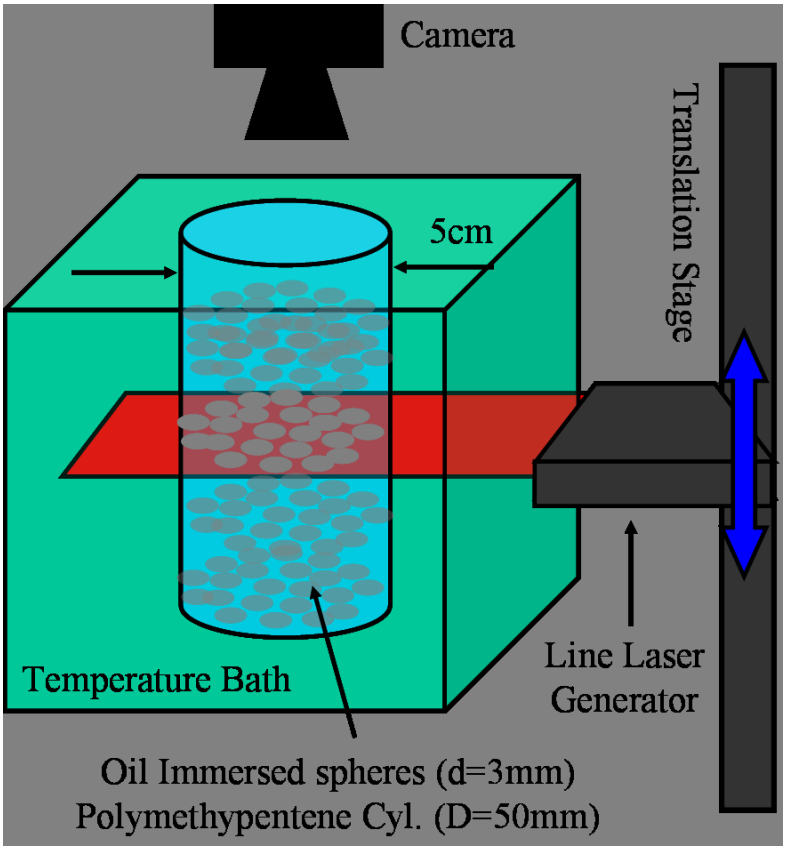

Figure 4.2: Temperature cycling setup.

4.4 Results-Vertical Tapping and Thermal Cycling

4.4.1 Jump Events in Vibration and Temperature Induced Compaction

A jump event is captured in Fig. 4.3. Frequencies of cage motion and jumps are shown in the graph, and a jump event is indicated in a cross sectional image of the interior obtained by confocal microscopy. The arrow points to the particle which fell from the upper layer to the lower layer during an oscillation. Compared to the average displacement of cage motion, $0.002d$, a jump event displaced the particle by $0.4d$.

The role of jumps has been investigated numerically by Ribiere *et al.* 100 jump events haven been observed in an assembly of 4096 particles subjected to 10000 taps in their Monte Carlo simulation. When displacements much larger than the mean cage motion are suppressed, slowed compaction of the material is observed. Packing fractions with and without inhibited jumps are plotted against the number of taps in Fig. 4.4. In this simulation result, the increase of packing fraction is slower in the system with inhibited jumps. Furthermore, the final packing fraction takes on a lower value when the jumps are inhibited. The jump events, therefore, though rare, plays a key role in the compaction mechanism of granular packings.

Compaction due to thermal cycling show similar results. Fig. 4.5 shows the jump events observed.

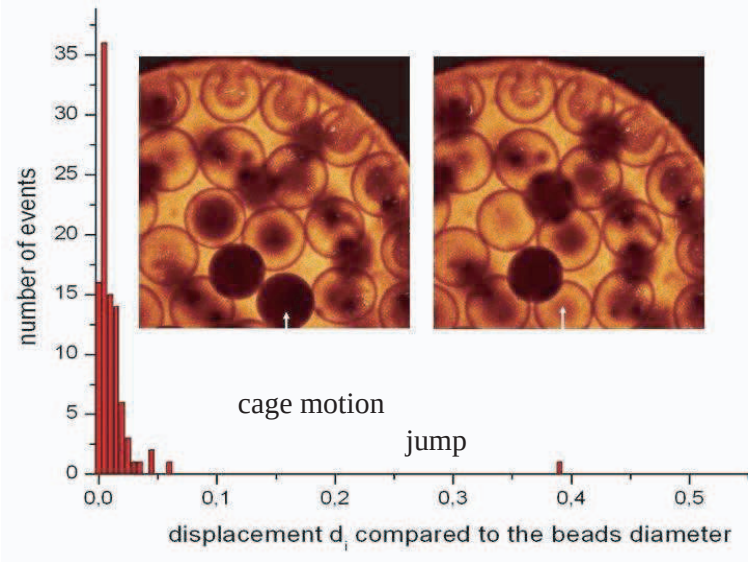

Figure 4.3: A rare event of jump is indicated by the arrow. The graph shows that this jump covers a displacement much greater than the predominant cage motion. Image obtained in collaboration with the Rennes group [9].

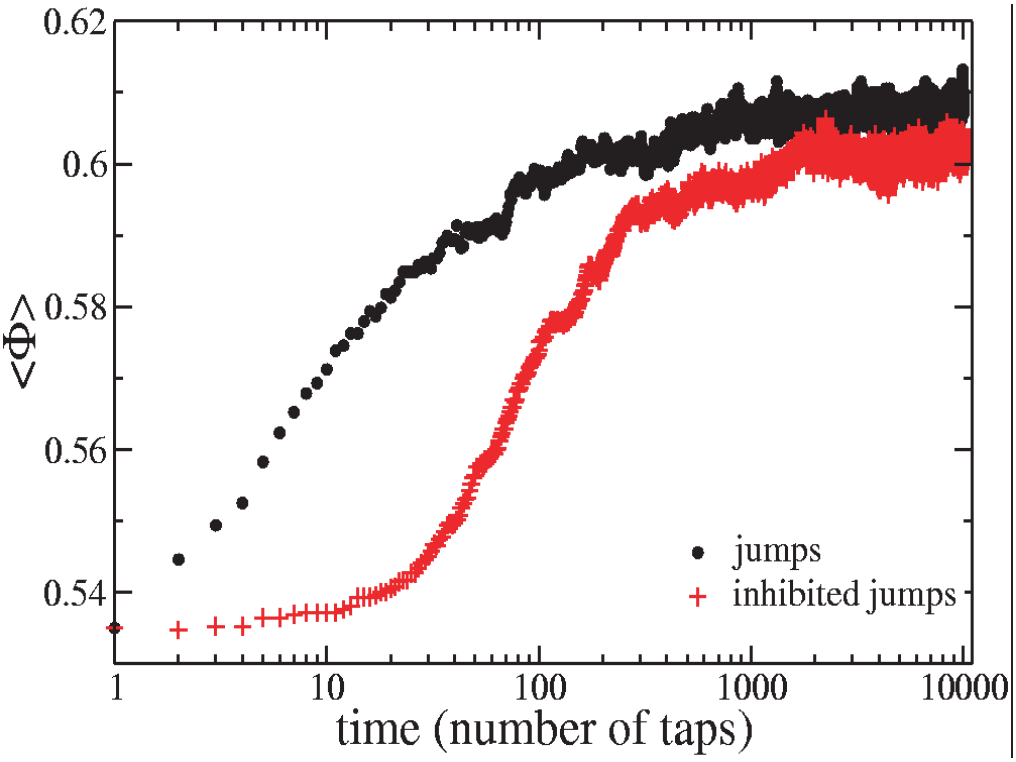

Figure 4.4: Simulation result by the Rennes researchers showing the evolution of packing fractions with and without jumps. The rare jumps play a key role in the compaction processes, as well as the the final packing fractions [9].

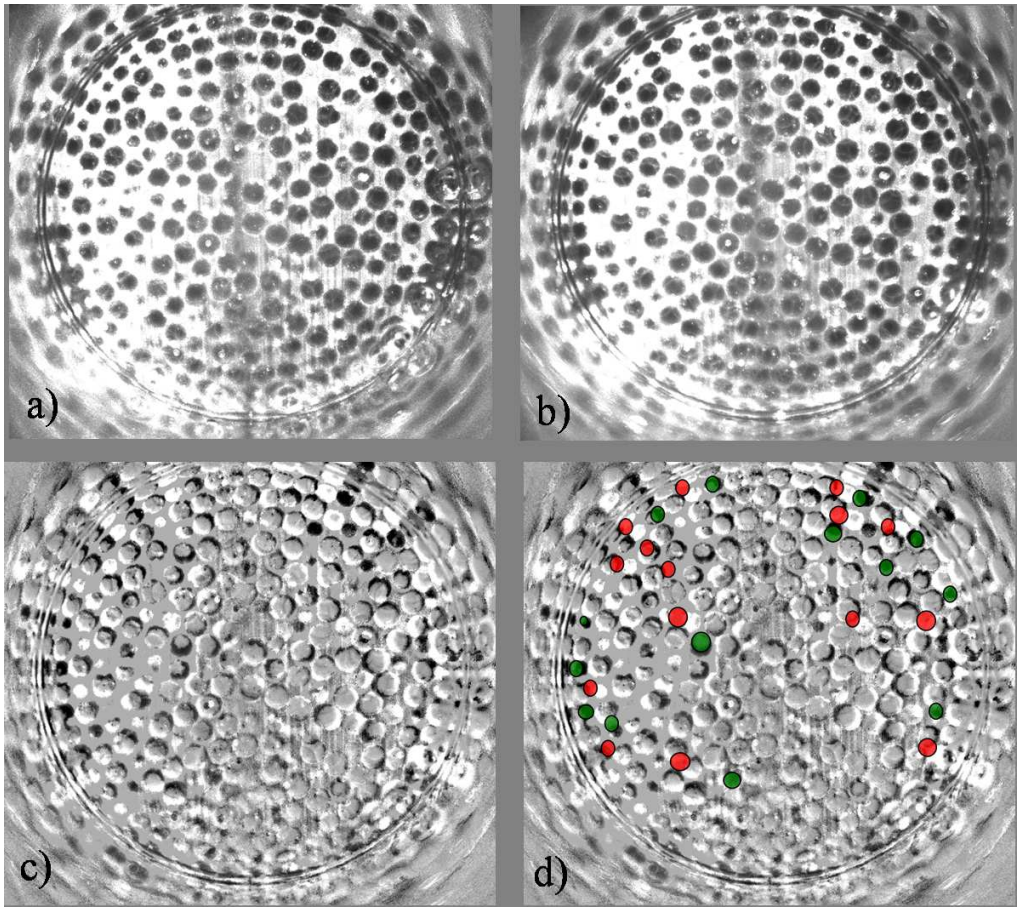

Figure 4.5: Cross sections before (a) and after (b) temperature cycling. Difference image (c) shows particles motion. The particles which came into the section after the cycle are shown in green, and the particles which left the section are marked in red (d).

4.4.2 Oscillatory Shear

We have seen in Chapter 2 that shear reversal causes transient increase in the material's packing fraction. Further compaction can be achieved by reversing the shearing direction after compaction has taken place and before the system dilates back to a steady state. Shearing direction can be reversed repeatedly after each height drop (oscillations). Fig. 4.6 shows the height of the material as a function of the oscillation number. The amount of compaction during each reversal gradually decreases. The functional form of the density increase can be fit equally well to the logarithmic law developed by Knight *et al.* [62] to describe compaction of granular material under tapping.

A stretched exponential, which may be used to describe the dynamics of jammed systems close to the glass transition as well as the tapped granular material mentioned above and in [65] also fits the experimental data well. Fit to the equation $h(x) = h_\infty + \Delta h * \exp\left[-\left(\frac{x+x_0}{\tau}\right)^\alpha\right]$, where x is the number of oscillations, is performed. Average values from fits yield $\alpha = 1.6 \pm 0.4$ and $\tau = 6.0 \pm 0.7$. Note that the compaction does not strongly depend on the oscillation amplitude, as long as the amplitude is larger than the characteristic length of $0.5d$ over which the system compacts during a single reversal (see Fig. 2.19).

Shear stress develops depending on the amplitude of oscillations as shown in Fig. 4.7. For small oscillation amplitude of $0.25d$, the shear stress remains below the steady state stress. For larger amplitudes, the shear stress gradually increases beyond the steady state values. Oscillation amplitudes larger than several particle

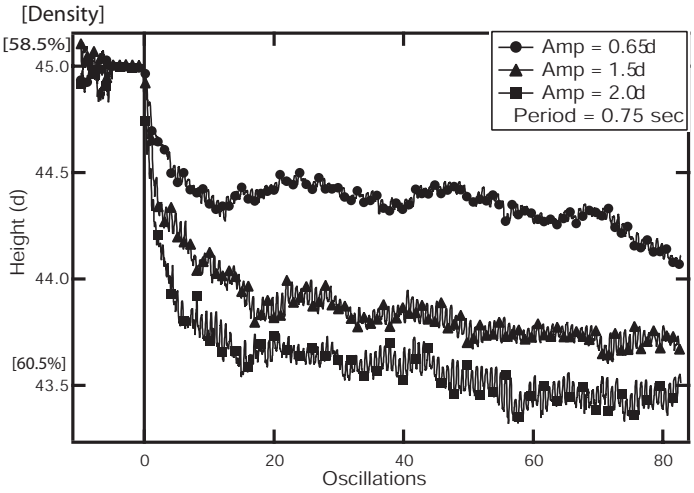

Figure 4.6: Evolution of packing fraction, or density, under repeated shear reversals as a function of the number of oscillations. Reversal of shear is repeated before full recovery takes place, resulting in further compaction. From [8].

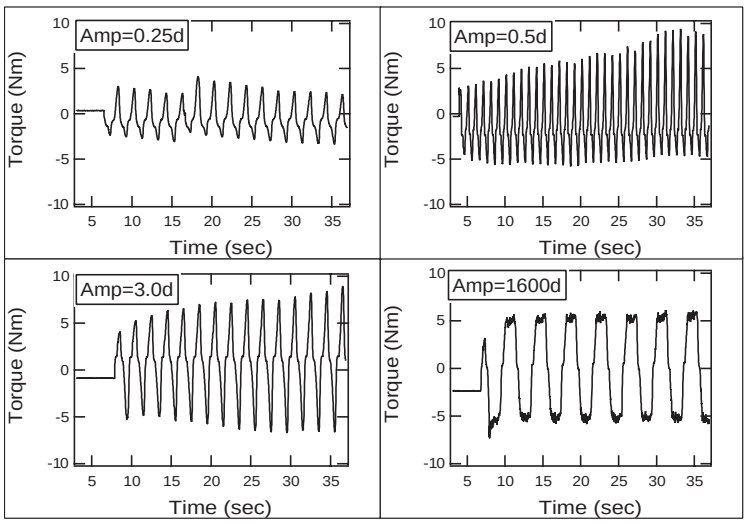

Figure 4.7: Shear stress as a function of time. Depending on the amplitude of oscillation, gradual strengthening in both directions was observed. From [8].

diameters erase the memory of prior shear, and thus the system reaches a steady state in both directions. Our results indicate that repeated reversals before reaching steady state gradually strengthen the material. Evolution of packing fraction is consistent with the force measurements.

Density measurements indicate that an additional slow transient exists, but the shear band during this slow transient does not differ appreciably from the steady state shear band. $l_e(r)$ is not strongly dependent of shear rates before and after reversal. We also found qualitatively similar results for $V(r)$ and l_e with a bottom connected to the inner cylinder, and when rotating the outer cylinder with the inner cylinder fixed.

4.5 Summary

Vibration, temperature cycling, and repeated shear reversals induce compaction in granular assemblies. The mechanisms at play are the cage motion and rare "jumps" in which a particle gains a displacement much larger than the average value. Evolution of packing fraction is a strong function of frequency of these jump events, as has been shown by simulation studies [9]. Repeated shear reversals, or oscillatory shear, have shown that the transient behavior at the onset of flow can take on a cumulative effect, thus causing overall compaction of the material.

4.6 Future Directions

Evolution of packing fraction due to temperature cycling in the above setup is a function of cycling temperature, ΔT and number of cycles, N. Large ΔT requires fewer number of cycles than small ΔT to achieve the same final packing fraction. Therefore it is possible to achieve the same packing fraction Φ through different combinations of these parameters. Here the author outlines a study of memory effect in granular compaction by temperature cycling.

Multiple samples are prepared to an identical packing fraction, Φ_i. They are subjected to different combinations of ΔT and N to reach Φ_f. The samples will have a preparation history of $(\Delta T_1, N_1), (\Delta T_2, N_2)$, etc. 3D image sequence is recorded after each cycling. These samples, now all having Φ_f but different preparation histories, are subjected to a new ΔT_f. The subsequent evolution of the packing fraction is monitored, and image sequences are recorded. The author conjectures that the samples which have been prepared through different paths evolve differently, depending on the preparation history. The author further speculates that jump events will play a more significant role in the compaction with large ΔT than with small ΔT, and as a result, two samples with identical packing fraction may have qualitatively different packing arrangement of particles. This difference may be reflected in the subsequent evolution of packing fraction.

Chapter 5

X-ray Microtomography

5.1 Motivations for X-ray Tomography

Non-invasive techniques for 3D imaging of granular material introduced in earlier chapters take advantage of index-matching fluids and transparent grains. Laser sheet scanning of fluid immersed grains has an advantage in that data acquisition and analysis are considerably simpler and faster than computed tomography methods with MRI or X-rays. Non-transparent materials such as real soil samples, however, cannot be imaged by this method. Furthermore, it is not clear whether the behavior of fluid immersed grains is identical to that of dry grains. Indeed, stress transmission characteristics in granular media depend strongly on coefficient of friction between grains. X-ray CT techniques for granular media allows for direct comparisons of fluid immersed and dry grains. Materials which cannot be used in laser sheet scanning, depending on their X-ray transmission characteristics, may be imaged with high resolution with X-ray microtomography method. As has been shown, investigation of microscopic origin of granular phenomena are essential in building models with predictive power.

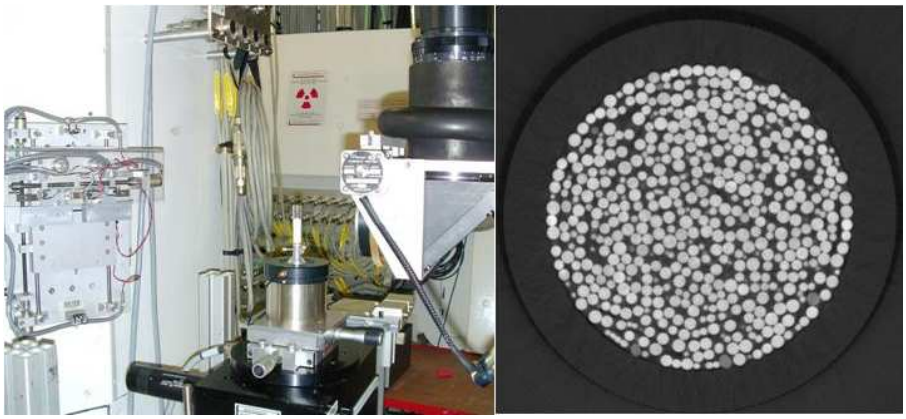

Figure 5.1: X-ray microtomography setup. The quartz cylinder mounted on the stage is filled with granular matter. A typical cross sectional image is shown on the right

5.2 X-ray Tomography at the ESRF

3D reconstruction techniques with X-ray microtomography have been explored by Richard, *et al.* [29]. X-ray imaging and tomography were carried out at the European Synchrotron Radiation Facility (ESRF) in collaboration with researchers from Universite de Rennes I. In order to draw comparisons with penetrometer experiment on fluid immersed glass spheres, $300\mu m$ glass spheres are put into a quartz cylinder with an internal diameter of $8mm$. Quartz was chosen for the container for its X-ray transmission qualities and better contrast with the sample. The experimental setup and a typical cross sectional image with spherical grains are shown in Fig. 5.1. The quartz container is seen mounted on a rotating stage. The experimental data were acquired at the ESRF's ID5 beam line with X-ray energy of 51keV.

Penetrometer testing of spherical particles at different stages of compaction

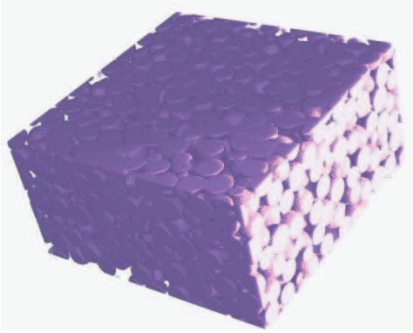

Figure 5.2: 3D reconstruction is performed on slices.

prepared by vertically tapping the samples at 4 and 6G have been carried out.

In addition, penetrometer testing of the lunar simulant, JSC-1, have been successfully imaged. As with the spherical particles, JSC-1 was subjected to vertical tapping, and particle motion due to penetrometer motion was recorded.

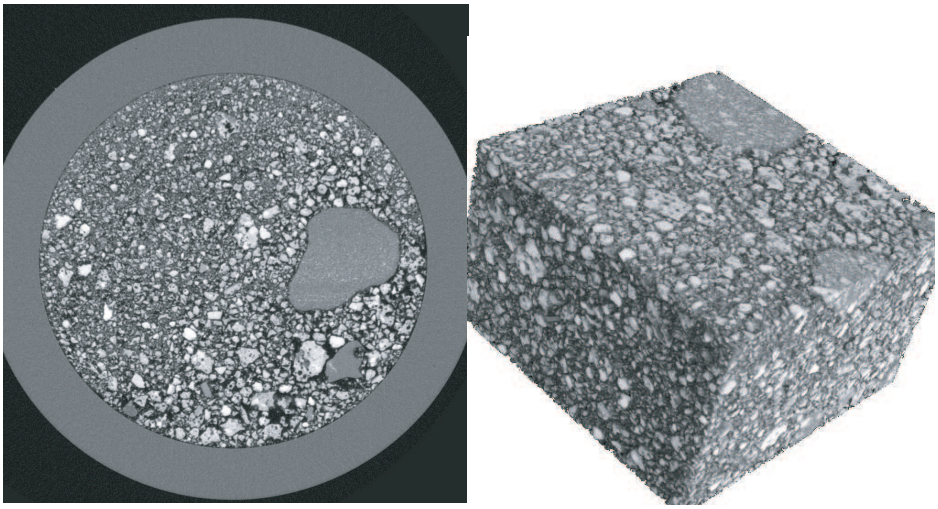

Figure 5.3: A cross section and a reconstructed view of the lunar simulant JSC-1. Smaller, non-spherical particles are clearly captured by the high resolution ($1\mu m$) X-ray system .

Bibliography

[1] Veit Schammle and H.J. Herrmann. Geomorphology: Solitary wave behaviour of sand dunes. *Nature*, 426:619–620, 2003.

[2] S. J. Friedmann, G. Kwon, and W. Losert. Granular memory and its effect on the triggering and distribution of rock avalanche events. *J. Geophys. Res.*, 108(B8):ECV8–1–11, 2005.

[3] $http://www.msss.com/mars_images/moc/june2000/nirgal/index.html$.

[4] H. Jaeger, S. Nagel, and R.P. Behringer. Granular solids, liquids, and gases. *Rev. Mod. Phys.*, 68(4):1259–73, 1996.

[5] $http://www.phy.duke.edu/\ bob/$.

[6] E. Hainbchner, S. Potthoff, H. Konietzky, and L te Kamp. *Numerical Modeling in Micromechanics via Particle Methods*. Balkema, 2002.

[7] T. S. Majmudar and R. P. Behringer. Contact force measurements and stress-induced anisotropy in granular materials. *Nature*, 435(7045):1079–1082, 2005.

[8] Masahiro Toiya, Justin Stambaugh, and Wolfgang Losert. Transient and oscillatory granular shear flow. *Phys. Rev. Lett.*, 93(8):088001/1–4, 2004.

[9] P. Ribiere, P. Richard, R. Delannay, D. Bideau, M. Toiya, and W. Losert. Effects of rare events on out of equilibrium relaxation. *cond-mat/0512403*, 2005.

[10] J. L. Heldman and M. T. Mellon. Observations of martian gullies and constraints on potential formation mechanisms. *Icarus*, 168(2):285–304, 2003.

[11] K. J. Kossacki and W. J. Markiewicz. Seasonal melting of surface water ice condensing in martian gullies. *Icarus*, 171(2):272–283, 2004.

[12] S. Deboeuf, E.M. Bertin, E. Lajeunesse, and O. Dauchot. Jamming transition of a granular pile below the angle of repose. *Eur. Phys. J. B*, 36:105–113, 2003.

[13] M Wormsbecker, A. Adams, T. Pugsley, and C. Winters. Segregation by size difference in a conical fluidized bed of pharmaceutical granulate. *Powder Technol.*, 153:72–80, 2005.

[14] H.P. Zhu and A.B. Yu. Micromechanic modeling and analysis of unsteady-state granular flow in a cylindrical hopper. *J. Eng. Math.*, 52:307–320, 2005.

[15] A. Wilkinson, R.P. Behringer, J.T. Jenkins, and M. Y. Louge. Granular materials and the risks they pose for success on the moon and mars. *AIP Conference Proceedings*, 746:1216–23, 2005.

[16] D. C. Hong and P. V. Quinn. Reverse brazil nut problem: Competition between percolation and condensation. *Phys. Rev. Lett.*, 86(15):3423–6, 2001.

[17] G. A. Canul-Chay, P. A. Belmont, Y. Nahmad-Molinari, and J. C. Ruiz-Suarez. Does the reverse brazil nut problem exist? *Phys. Rev. Lett.*, 89(18):189601, 2002.

[18] T. Shinbrot. The brazil nut effect-in reverse. *Nature*, 429:352–3, 2004.

[19] M. Tarzia, A Fierro, M. Nicodemi, M. Ciamarra, and A. Coniglio. Size segregation in granular media induced by phase transition. *Phys. Rev. Lett.*, 95(7):0778001–01 to 04?, 2005.

[20] H. Walliser. Comment on reverse brazil nut problem: Competition between percolation and condensation. *Phys. Rev. Lett.*, 89(18):189603, 2002.

[21] R. Khosropour, J. Zirinsky, H. K. Pak, and R. P. Behringer. Convection and size segregation in a couette flow of granular material. *Phys. Rev. E.*, 56(4):4467–73, 1997.

[22] A. Barrat and V. Loreto. Memory in aged granular media. *Eur. Phys. Lett.*, 53(2):297–303, 2000.

[23] C. Josserand, A.V. Tkachenko, D.M. Mueth, and H.M. Jaeger. Memory effects in granular materials. *Phys. Rev. Lett.*, 85(17):3632–6, 2000.

[24] K. M. Hill, A. Caprihan, and J. Kakalios. Bulk segregation in rotated granular material measured by magnetic resonance imaging. *Phys. Rev. Lett.*, 78(1):50–53, 1997.

[25] J. C. Tsai, G.A. Voth, and J.P. Gollub. Internal ganular dynamics, shear-induced crystallization, and compaction steps. *Phys. Rev. Lett.*, 91(6):064301–1–063301–4, 2003.

[26] D.M. Mueth, G.F. Debregeas, G.S. Karczmart, P.J. Eng, S R. Nagel, and H.M. Jaeger. Signatures of granular microstructure in dense shear flows. *Nature*, 406:385–9, 2000.

[27] T. Aste, M. Saadatfar, and T. J. Senden. Geometrical structure of disordered sphere pakcings. *Phys. Rev. E.*, 71(6):061302–1 to 14, 2005.

[28] E. Caglioti, A. Coniglio, H. J. Herrmann, V. Loreto, and M. Nicodemi. Cooperative length approach for granular media. *Physica A*, 265(1-2):311–8, 1999.

[29] P. Richard, P. Philippe, F. Barbe, S. Bourles, X. Thibault, and D. Bideau. Analysis by x-ray microtomography of a granular packing undergoing compaction. *Phys. Rev. E.*, 68:020301–1/4, 2003.

[30] M. Babic. Unsteady couette granular flows. *Phys. Fluids*, 9(9):2486–505, 1997.

[31] R.A. Bagnold. The shearing and dilatation of dry sand and the 'singing' mechanism. *Proceedings of the Royal Society of London. Series A, Mathematical and Physical Sciences*, 295(1442):219–232, 1966.

[32] E. Clement. Rheology of granular media. *Current Opinion in Colloid and Interface Science*, 4(4):294–9, 1999.

[33] J.T. Jenkins and S.B. Savage. A theory for the rapid flow of identical, smooth, nearly elastic, spherical particles. *J. of Fluid Mech.*, 130:187–202, 1983.

[34] W. Losert, L. Bocquet, T.C. Lubensky, and J.P. Gollub. Particle dynamics in sheared granular matter. *Phys. Rev. Lett.*, 85(7):1428–31, 2000.

[35] W. Losert and G. Kwon. Transient and steady state dynamics of granular shear flows. *Advances in Complex Systems*, 4:369–76, 2001.

[36] Junfei Geng, D. Howell, E. Longhi, and R. P. Behringer. Footprints in sand: The response of a granular material to local perturbations. *Phys. Rev. Lett.*, 87(3):03556, 2001.

[37] D. Howell and R.P. Behringer. Stress fluctuations in 2d granular couette experiment: A continuous transition. *Phys. Rev. Lett.*, 82(26):5241–5244, 1999.

[38] B. Utter and R.P. Behringer. Transients in sheared granular matter. *Eur. Phys. J. B*, 14(4):373–380, 2004.

[39] M. Bolton. *A Guide to Soil Mechanics*. Macmillan Education Ltd, 1979.

[40] G. B. Sowers and G. F. Sowers. *Introductory Soil Mechanics and Foundations*. The MacMillan Company, 1970.

[41] R.P. Behringer, D. Howell, L. Kondic, S. Tennakoon, and C. Veje. Predictability and granular materials. *Physica D*, 133(1-4):1–17, 1999.

[42] J. C. Tsai, G.A. Voth, and J.P. Gollub. Mixing of granular materials: A test-bed for dynammical system for pattern formation. *Phys. Rev. Lett.*, 9(8):1467–1484, 1999.

[43] D. Fenistein, J.W. van de Meent, and M. van Hecke. Universal and wide shear zones in granular bulk flow. *Phys. Rev. Lett.*, 87(17):178305–1–178305–4, 2001.

[44] F. Gadala-Maria and A. Acrivos. Shear-induced structure in a concentrated suspension of solid spheres. *J. Rheol.*, 24(6):799–814, 1980.

[45] Loic Vanel, Daniel Howell, D. Clark, R. P. Behringer, and Eric Clement. Memories in sand: Experimental tests of construction history of stress distributions under sandpiles. *Phys. Rev. E.*, 60:R5040–3, 1999.

[46] K. Terzaghi and R.B. Peck. *Soil Mechanics in Engineering Practice*. John Wilen & Sons, Inc., 2 edition, 1967.

[47] GDR MiDi. On dense granular flows. *Eur. Phys. J. E.*, 14:341–365, 2004.

[48] R. F. Scott, III W. D. Carrier, N. C. Costes, and J.K. Mitchell. Apollo 12 soil mechanics investigation. *Geotechnique*, 21(1):1–14, 1971.

[49] P. van den Berg. *Analysis of Soil Penetration*. Delft University Press, 1994.

[50] H. S. Yu and J. K. Mitchell. Analysis of cone resistance: Review of methods. *J. Geotech. Geoenviron.*, 124:140–149, 1998.

[51] B. Utter and R.P. Behringer. Self-diffusion in dense granular shear flows. *Phys. Rev. E.*, 69(3):31308/1–12, 2004.

[52] J. Duran. *Sands, Powders, and Grains: An Introduction to the Physics of Granular Materials*. Springer-Verlag, 1999.

[53] M. B. Stone, R. Barry, D. P. Bernstein, M. D. Pelc, Y. K. Tsui, and P. Schiffer. Local jamming via penetration of a granular medium. *Phys. Rev. E.*, 70(4):41301–1–10, 2004.

[54] M. B. Stone, D. P. Bernstein, R. Barry, M. D. Pelc, Y. Tsui, and P. Schiffer. Getting to the bottom of granular medium. *Nature*, 427:503–504, 2004.

[55] Samer Sadek, Magued G. Iskander, and Jinyuan Liu. Accuracy of digital image correlation for measuring deformations in transparent media. *J. Comput. Civil. Eng.*, 17:88–96, 2003.

[56] Magued G. Iskander, Jinyuan Liu, and Samer Sadek. Transparent amorphous silica to model clay. *J. Geotech. Geoenviron.*, 128(3):262–273, 2002.

[57] A. L. Welker, J. J. Bowders, and R. B. Gilbert. Applied research using a transparent material with hydraulic properties similar to soil. *Geotech. Test. J.*, 22(3):266–270, 1999.

[58] M. B. Stone, D. P. Bernstein, R. Barry, M. D. Pelc, Y. Tsui, and P. Schiffer. Unpublished. 2004.

[59] K. M. Hill and J. Kakalios. Axial segregation of granular media rotated in a drum mixer: Pattern evolution. *Phys. Rev. E.*, 56(4):4386–4393, 1997.

[60] D. V. Khakhar, A. V. Orpe, and S. K. Hajra. Segregation of granular materials in rotating cylinders. *Physica A*, 318(1-2):129–136, 2003.

[61] M. Y. Louge. Model for dense granular flows down bumpy inclines. *Phys. Rev. E.*, 67(6):61303/1–11, 2003.

[62] J.B. Knight, C.G. Fandrich, C.N. Lau, H.M. Jaeger, and S.R. Nagel. Density relaxation in a vibrated granular medium. *Phys. Rev. E.*, 51(5):3957–63, 1995.

[63] P. Philippe and D. Bideau. Compaction dynamics of a granular medium under vertical tapping. *Eur. Phys. Lett.*, 60(5):677–683, 2002.

[64] P. Schiffer. Unpublished. 2006.

[65] J.C. Phillips. Strtched exponential relaxation in molecular and electronic glasses. *Rep. Prog. Phys.*, 59:1133–207, 1996.